SCIENCE CHINA Materials REVIEWS

mater.scichina.com link.springer.com

Published online 10 September 2020 | https://doi.org/10.1007/s40843-020-1452-9

Sci China Mater 2021, 64(1): 1–26

Recent progresses of micro-nanostructured transition metal compound-based electrocatalysts for energy conversion technologies

Jiajun Wang[1], Zhao Zhang[1], Jia Ding[1], Cheng Zhong[1], Yida Deng[1], Xiaopeng Han[1*] and Wenbin Hu[1,2*]

ABSTRACT **The rapid consumption of fossil fuels has caused increasingly climatic issues and energy crisis, which leads to the urgent demand for developing sustainable and clean energies. Electrocatalysts play a key role in the development of electrochemical energy conversion and storage devices. Especially, developing efficient and cost-effective catalysts is important for the large-scale application of these devices. Among various electrocatalyst candidates, earth abundant transition metal compound (TMC)-based electrocatalysts are being widely and rapidly studied owing to their high electrocatalytic performances. This paper reviews the recent and representative advances in efficient TMC-based electrocatalysts (i.e., oxides, sulfides, selenides, phosphides, carbides and nitrides) for energy electrocatalytic reactions, including hydrogen evolution reaction (HER), oxygen evolution reaction (OER) and oxygen reduction reaction (ORR). Different compounds with different applications are summarized and the relative mechanisms are also discussed. The strategies for developing earth-abundant and low-cost TMC-based electrocatalysts are introduced. In the end, the current challenges and future perspectives in the development of TMC research are briefly discussed. This review also provides the latest advance and outlines the frontiers in TMC-based electrocatalysts, which should provide inspirations for the further development of low-cost and high-efficiency catalysts for sustainable clean energy technologies.**

Keywords: energy electrocatalysis, transition metal compounds, HER, OER, ORR

INTRODUCTION

The rapidly increasing consumption of fossil fuels (e.g., coal, petroleum and natural gas) is causing a series of climatic issues and seriously damaging the global environment [1–3]. Developing renewable and environment-friendly energy systems has shown promising prospects for the sustainable development of human society [4–7]. Among various strategies, the electrochemical energy conversion and storage devices have drawn great attentions due to their low carbon emissions and high energy densities [8]. Typically, these devices with different applications usually involve different electrochemical reactions, such as hydrogen evolution reaction (HER), oxygen evolution reaction (OER), oxygen reduction reaction (ORR), CO_2 electroreduction reaction (CO_2RR) and alkohol electrooxidation reaction (AOR) [9–12]. Therefore, it is critical to improve the kinetics and reduce the power consumptions of these reactions for high device performances. Electrocatalysts play a critical role in enhancing reaction rates *via* facilitating the conversion of reaction intermediates and reducing the resistance [13,14]. Noble metals have been regarded as the state-of-art electrocatalysts for HER (Pt), OER (Ir/Ru oxide) and ORR (Pt) [15,16]. However, the high cost and limited resources still hinder their large-scale commercialization.

Considering the cost and reducing the dependency of noble metals, great efforts have been tried to develop nonprecious metal-based electrocatalysts, such as transition metal-based, transition metal compound (TMC)-based and carbon-based nanomaterials [8,17]. Especially,

[1] School of Materials Science and Engineering, Tianjin Key Laboratory of Composite and Functional Materials, Key Laboratory of Advanced Ceramics and Machining Technology (Ministry of Education), Tianjin University, Tianjin 300072, China

[2] Joint School of National University of Singapore and Tianjin University, International Campus of Tianjin University, Binhai New City, Fuzhou 350207, China

* Corresponding authors (emails: xphan@tju.edu.cn (Han X); wbhu@tju.edu.cn (Hu W))

TMCs (such as oxides, sulfides, selenides, phosphides, carbides and nitrides) have shown promising prospects in different applications. For example, MoS_2 has been proved to be a promising HER electrocatalyst with highly active edge sites [18], Co_3O_4 has been widely used for OER in alkaline electrolytes [19], and $ZnMnCoO_4$ has shown comparable ORR activity to commercial Pt/C with high stability in alkaline electrolyte [20]. However, there are still some critical issues that significantly hinder the practical commercialization of TMC-based electrocatalysts [21,22]: 1) the activities of most TMC-based electrocatalysts are still not comparable to precious metal-based catalysts and cannot meet practical applications. For example, industrial electrolyzers require an overpotential of 300 mV to reach a high current density of 500 mA cm^{-2}, while it is difficult for most of the reported TMC-based electrocatalysts to meet this requirement. 2) In industrial applications, the electrodes should keep stable at 500 mA cm^{-2} for thousands of hours, while most of the TMC-based electrocatalysts are far from satisfactory due to the structure/composition evolution. Moreover, the intrinsic stability of TMCs would be significantly affected by the aging and polarizing in strong acid/alkaline environment. For example, many TMC-based electrocatalysts show inferior corrosion resistance in the acid electrolytes or under high overpotentials [17]. Due to the surface change during the oxidization/reduction reaction, it is difficult to distinguish the actual active sites of TMCs during the reaction and clarify the reaction mechanisms, which significantly hinder the further improvement of the corresponding electrocatalysts [8]. 3) It has been widely accepted that nano-sized electrocatalysts outperform bulk materials owing to the significantly increased electrochemical surface area (ECSA) and active sites. However, the current industrial preparation of TMCs still employs the gas-solid method, and therefore most of the products are bulks with low electrocatalytic performances. Although the unit prices of bulk TMCs are lower than those of precious metals, their inferior electrocatalytic performances seriously restrict the practical applications. On the other hand, numerous TMC-based electrocatalysts with high activities have been fabricated using hydrothermal, solvothermal and chemical vapor deposition (CVD) methods, while the amplification of large-scale preparation from laboratorial to industrial scale is still a critical problem due to the cost and technological problems.

To meet the current challenges and promote the practical applications of TMC-based electrocatalysts, various design strategies are proposed, including exploring new active sites, increasing ECSA to expose more active sites, improving the intrinsic activity of active site and enhancing the electron transfer [4,23,24]. As the studies of TMCs for electrocatalysis are being reported rapidly in recent years, there are already many comprehensive reviews about the catalyst design and mechanism. This mini-review aims to summarize the most recently reported advances (since 2018) about TMC-based electrocatalysts for HER, OER, ORR and the relevant devices (such as water splitting devices and Zn-air batteries), and outline the frontiers of this field. At first we briefly introduce the basic characteristics of HER, OER and ORR. Then the selected progresses of transition metal oxides, sulfides, selenides, phosphides, carbides and nitrides for the aforementioned electrocatalytic reactions are comprehensively reviewed. Meanwhile, the new strategies and relevant reaction mechanisms of different electrocatalysts are also summarized (Fig. 1). Finally, the remaining challenges for the further development of TMC-based electrocatalysts are discussed. This review introduces the applicable methods for tuning the physiochemical properties (component, micro/nanostructure and electron distribution) of TMCs, which contributes to developing novel, low-cost and earth-abundant energy electrocatalytic nanomaterials. Moreover, the strategies for optimizing the adsorption/desorption properties, facilitating the charge and mass transfer, and finally enhancing the electrocatalytic performances are also discussed, which

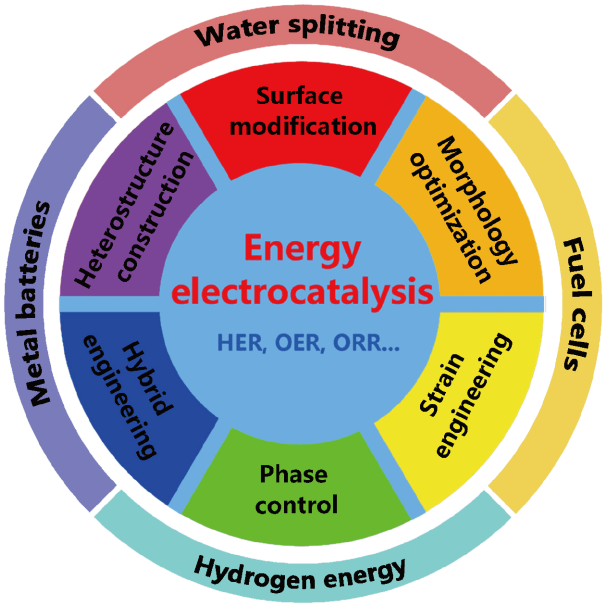

Figure 1 Schematic illustration of the strategies for enhancing the electrocatalytic performance of TMC-based electrocatalysts.

provides inspirations for further exploring highly efficient electrocatalysts and promoting the practical device applications for energy storage and conversion.

ELECTROCHEMISTRY OF HER, OER AND ORR

HER

The multiple elementary steps of HER are as follows [25]:

Volmer step:

$$H^+ + * + e^- \rightarrow H^* \text{ (acid)}, \quad (1)$$

$$H_2O + * + e^- \rightarrow H^* + OH^- \text{ (alkaline)}; \quad (2)$$

Heyrovsky step:

$$H^* + e^- + H^+ \rightarrow H_2 + * \text{ (acid)}, \quad (3)$$

$$H^* + e^- + H_2O \rightarrow H_2 + * + OH^- \text{ (alkaline)}; \quad (4)$$

Tafel step:

$$H^* + H^* \rightarrow H_2 + 2^*, \quad (5)$$

where * represents the surface catalytic site. For acid HER, at the first step (Volmer step), a proton is reduced on the active site, which forms an adsorbed H. While for alkaline HER, a H_2O dissociation step has to proceed to provide a proton before the proton reduction and adsorption, which makes the kinetics more sluggish than acid HER. In the second step, an H^* will react with another proton and electron to form a hydrogen molecule when the surface H coverage is low (Volmer-Heyrovsky reaction). While two adjoining H^* will directly bind with each other to generate H_2 if the H coverage is high (Volmer-Tafel reaction). Moreover, both the two reaction pathways involve the formation of H^*, which plays a critical role in determining the reaction rate. Typically the Gibbs free energy change for H^* (ΔG_{H^*}) reflects the intrinsic HER activity and an ideal ΔG_{H^*} should be close to zero [26].

OER and ORR

OER involves four elementary steps [27]:

$$OH^- + * \rightarrow e^- + OH^*, \quad (6)$$

$$OH^* + OH^- \rightarrow O^* + e^- + H_2O, \quad (7)$$

$$O^* + OH^- \rightarrow e^- + OOH^*, \quad (8)$$

$$OOH^* + OH^- \rightarrow O_2 + * + e^- + H_2O. \quad (9)$$

From the equations above, more electrons and reaction intermediates are involved in OER than HER, which makes OER more kinetically sluggish. As there are three intermediates (OH^*, O^* and OOH^*) formed during OER and all of the steps are thermodynamically uphill, the step with the highest barrier determines the overall OER rate. Therefore, the binding strength between the intermediates and the active sites significantly affect the reaction kinetics. On the other hand, although the reaction mechanism of acid OER is similar to that of alkaline OER, only RuO_2 and IrO_2 show satisfactory performances in acid electrolyte, as the strongly oxidizing and acid environment can easily damage most of the TMCs [28]. Therefore, most of the remarkable TMC-based electrocatalysts are applied in alkaline electrolytes.

Similar to OER, most of the ORR electrocatalysts show more efficient performances in alkaline than acid environment. There are two possible ORR reaction pathways in alkaline electrolyte [29]:

(i) Direct $4e^-$ pathway:

$$O_2 + 4e^- + 2H_2O \rightarrow 4OH^-. \quad (10)$$

(ii) $2e^-$ to HO_2^-:

$$O_2 + H_2O + 2e^- \rightarrow HO_2^- + OH^-. \quad (11)$$

Followed by further reduction or decomposition of HO_2^-:

$$HO_2^- + H_2O + 2e^- \rightarrow 3OH^- \text{ or } 2HO_2^- \rightarrow 2OH^- + O_2. \quad (12)$$

Therefore, the $4e^-$ pathway is kinetically faster than $2e^-$ pathway and most of the TMC-based electrocatalysts with high efficiency follow the $4e^-$ pathway. Similar to OER, the adsorption strength of the intermediates (OH^*, O^* and OOH^*) also critically affects the ORR rate [30].

In summary, although the specific elementary steps of HER, ORR and OER are different, it is clear that the intrinsic reaction activities of HER, OER and ORR are significantly related with the adsorption properties of intermediates on the surface active sites. For example, if HER intermediates bind to the catalytic sites too weakly, the adsorption step (Volmer step) will be hindered and significantly inhibits the following steps. While if the intermediates bind to the surface too strongly, it will be difficult to form products (hydrogen) with smooth desorption from the active sites. Namely, an ideal catalyst should have a suitable binding strength for intermediates in each elementary step: neither too strong nor too weak. By plotting experimental electrochemical activities against the calculated Gibbs free energy (ΔG) by the density functional theory (DFT), a volcano relationship can be established. Fig. 2 shows some typical volcano plots related with HER, OER and ORR, which clearly show the relationship between the ΔG and the catalytic activity. Therefore, the free energy is regarded as a useful factor for predicting and explaining the electrocatalytic activities, which has been widely applied in electrocatalytic studies.

ELECTROCATALYSTS FOR HER, OER, ORR AND RELEVANT ENERGY CONVERSION DEVICES

Various TMC-based electrocatalysts, including oxides,

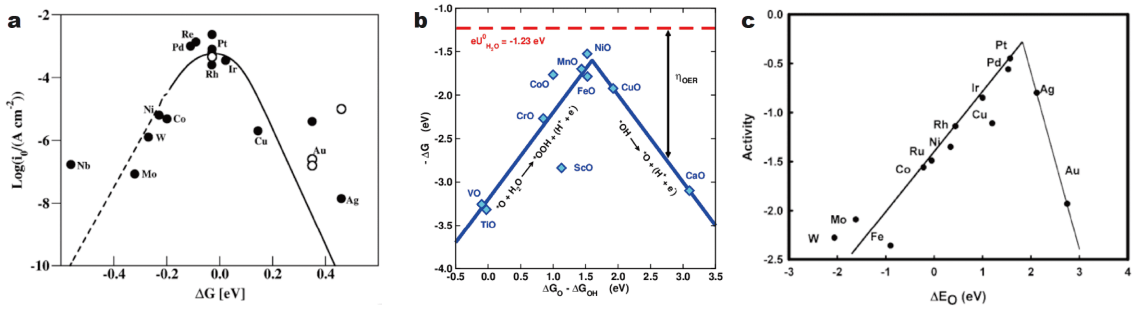

Figure 2 (a) HER, (b) OER, and (c) ORR volcano plots for different electrocatalysts. Reprinted with permission from Ref. [31] (Copyright 2010), [32] (Copyright 2015) and [33] (Copyright 2004), American Chemical Society, respectively.

sulfides, selenides, phosphodes, carbides and nitrides, have been applied in electrocatalytic reactions in recent years. Compared with other compounds (e.g., halogenides, borides and arsenides), these compounds are more promising since the preparation procedures are more facile and safe without using highly toxic non-metallic precursors (e.g., As, HF, HCl and HBr), and the synthesis methods have been widely developed (such as hydrothermal, solvothermal and annealing methods). Moreover, it is easier to controllably synthesize these TMC-based compounds with tunable phase and composite than other compounds, which would lead to significantly altered physiochemical properties and electrochemical performances. Up to date, many earth-abundant and low-cost catalysts have shown excellent electrocatalytic performances which are comparable to noble metals, while the property of each kind of compound is different and the corresponding fabrication strategy and reaction mechanism are also different. This part will summarize recent and representative advances of TMCs classified by non-metallic elements and the optimization strategies are also discussed.

Transition metal oxides

Transition metal oxide-based electrocatalysts have been widely developed owing to their low toxicity, low cost and abundant reserves [34]. Moreover, owing to the surface oxygen-containing groups and the different cationic oxidation states of transition metals, the adsorption and activation of oxygen molecules on the oxide surface are naturally suitable [35]. However, their poor electron transfer ability and limited intrinsic activity are still needed to be further improved. Many efforts are made to improve their hydrogen and oxygen electrocatalytic activities *via* various design strategies [36–40]. Exposing facets with higher electrocatalytic activity has been proved to be an effective way for improving the performance. Han *et al.* [41] prepared crystallized Co_3O_4 nanomaterials with exposed planes ({001}, {001} + {111}, and {112}) *via* a facile and template-free hydrothermal strategy. In {001} and {111} planes, Co ions occupy the tetrahedral coordination (Co^{2+}Td) (Fig. 3a). While in {112} plane, Co ions occupy not only tetrahedral coordination but also octahedral coordination (Co^{3+}Oh). According to the ligand field theory, Co^{3+}Oh has a stronger electron donating ability and therefore is beneficial for the reduction of –OH and O_2^{2-}. Furthermore, DFT calculations reveal that {112} surface has a moderate oxygen binding ability compared with {001} and {111} planes. As a result, the {112} faceted Co_3O_4 electrocatalyst showed high ORR performance with a diffusion-limited current density of 5.48 mA cm^{-2} and a smaller Tafel slope (62 mV dec^{-1}) than that of Pt/C (69 mV dec^{-1}) (Fig. 3b). Anion/cation doping has been widely applied for tuning the intrinsic activity of catalytic sites [42]. Peng *et al.* [43] prepared highly porous S-doped $CaMnO_3$ (CMO) nanotubes *via* combining electrospinning, heat calcination, and sulfurization treatment, in which sulfur was doped onto the surface of $CaMnO_3$ nanotubes to engineer the electronic and defective properties of the pristine material. After the introduction of sulfur, the intrinsic conductivity and oxygen vacancies were significantly increased, which helped to enhance the electron transfer and increase the exposure of catalytic sites during the reaction. Moreover, the DFT calculations revealed that the adsorption properties of the reaction intermediates were significantly optimized by the sulfur dopants. As a result, the as-prepared CMO/S nanomaterials showed significantly enhanced OER ($E_{j=10\ mA\ cm^{-2}}$=1.7 V *vs.* RHE) and ORR (E_{half} =−0.760 V *vs.* RHE) performances in alkaline electrolyte. Moreover, the CMO/S-based rechargeable Zn-air battery exhibited an outstanding performance. Li *et al.* [44] investigated the effect of N dopants on the OER activity of N-doped Co_3O_4 nanostructures (N-Co_3O_4), which was

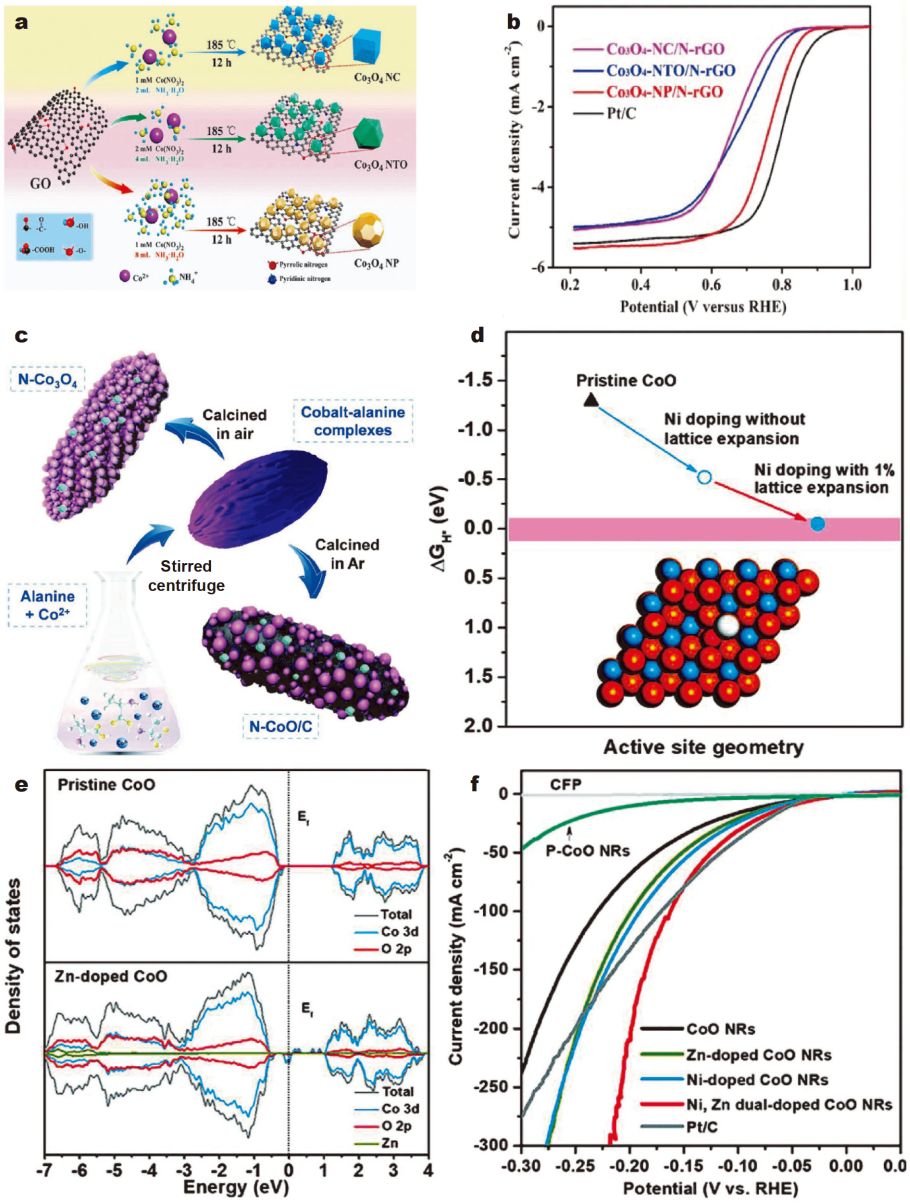

Figure 3 (a) Schematic illustration for preparation of different Co_3O_4 electrocatalysts, (b) linear sweep voltammetry (LSV) of different samples at 1600 rpm in O_2-saturated 0.1 mol L^{-1} KOH solution. Reprinted with permission [41]. Copyright 2018, Wiley. (c) A simple synthesis scheme of the as-prepared samples. Reprinted with permission [44]. Copyright 2018, Wiley. (d) DFT calculated hydrogen adsorption free energy, ΔG_{H^*}, on pristine CoO, Ni-doped CoO (with ~11% surface Ni dopant concentration), and the strained Ni-doped CoO (with 1% tensile strain), (e) Density of states of pristine CoO and Zn-doped CoO (with ~2% Zn dopant concentration), (f) LSVs of different catalysts recorded in 1 mol L^{-1} KOH. Reprinted with permission [45]. Copyright 2019, Wiley.

prepared *via* the pyrolysis of cobalt-alanine complexes in air (Fig. 3c). DFT calculations demonstrated that the O–H bond of the intermediate OH^- on N-Co_3O_4 was 0.99 Å and longer than that on Co_3O_4 (0.98 Å), indicating stronger adsorption of OH^- and the OER kinetics was therefore boosted. Moreover, the bandgap was significantly narrowed from 1.80 to 1.42 eV on N-Co_3O_4, and the charge transfer was facilitated during the reaction. Ling *et al.* [45] developed Ni, Zn co-doped CoO nanorods as HER electrocatalysts using a cation exchange strategy and different cations were found to play different roles in enhancing the HER performance. Due to the DFT calculations, compared with unmodified CoO, more electrons migrated to the surface O in Ni-CoO from the

neighboring Ni, which helped to weaken the binding strength between adsorbed hydrogen and active sites. Therefore, the ΔG_{H^*} was significantly reduced to an ideal value (−0.05 eV) (Fig. 3d). On the other hand, the projected density of state (PDOS) results revealed a significantly increased conductivity and carrier concentration in Zn-CoP (Fig. 3e), which facilitated the electron transfer from the electrode to the surface catalytic sites. The HER activity of the as-prepared Ni, Zn-CoO nanorods was superior to many reported metal oxides with an overpotential of 79 mV at 20 mA cm^{-2} (Fig. 3f). Zhao *et al.* [46] prepared Co-MnO_2|OV ultrathin nanosheets (NSs) through a spontaneous redox reaction between Co/NCNFs and $KMnO_4$. Compared with the unmodified MnO_2, the Co dopants led to the formation of Co-MnO_2|OV ultrathin NSs and a large amount of oxygen vacancies were *in-situ* formed during the preparation process. Owing to the advantageous structural properties, faster charge transfer and higher exposure of catalytic sites were achieved. On the other hand, the DFT calculations demonstrated that the electrons were more delocalized on Co-MnO_2|OV, which led to a higher electronegativity and increased charge transfer ability. Meanwhile, the calculation of free energy change revealed that the energy barrier of the rate-determining step was reduced after the introduction of Co dopant and oxygen vacancies on MnO_2. Finally, the Co-MnO_2|OV showed a good OER with 10 mA cm^{-2} at 279 mV. Liu *et al.* [47] prepared an ultrathin amorphous cobalt–vanadium hydr(oxy)oxide (CoV-UAH) by dropping an alkaline solution with ammonium metavanadate into an aqueous cobaltous solution. The *in-situ* X-ray absorption near edge structure (XANES) spectra demonstrated that the introduction of V significantly promoted the formation of the real OER catalytic sites (CoOOH). Meanwhile, the electrochemical impedance spectroscopy (EIS) data demonstrated an enhanced charger transfer ability on CoV-UAH, which was owing to the ultrathin nanostructure and abundant catalytic sites. Moreover, the DFT calculations revealed that the energy barrier of elementary step on Co site was optimized by the neighboring V atom, thus the intrinsic activity was also enhanced. As a result, the CoV-UAH required only 250 mV to reach 10 mA cm^{-2}, which was a remarkable OER activity in alkaline electrolyte.

Constructing hybrid nanomaterials with heterostructures is another strategy for enhancing the electrocatalytic performance [48,49]. Yan *et al.* [50] engineered a nanocrystalline CeO_2/amorphous $Ni(OH)_2$ hybrid ($NiCeO_xH_y$) for alkaline *via* an electrochemical deposition method (Fig. 4a). As a result, the $NiCeO_xH_y$ electrode outperformed the commercial RuO_2 with an overpotential of 177 mV at 10 mA cm^{-2} and a high stability over 300 h at 1000 mA cm^{-2} (Fig. 4b). It was found that

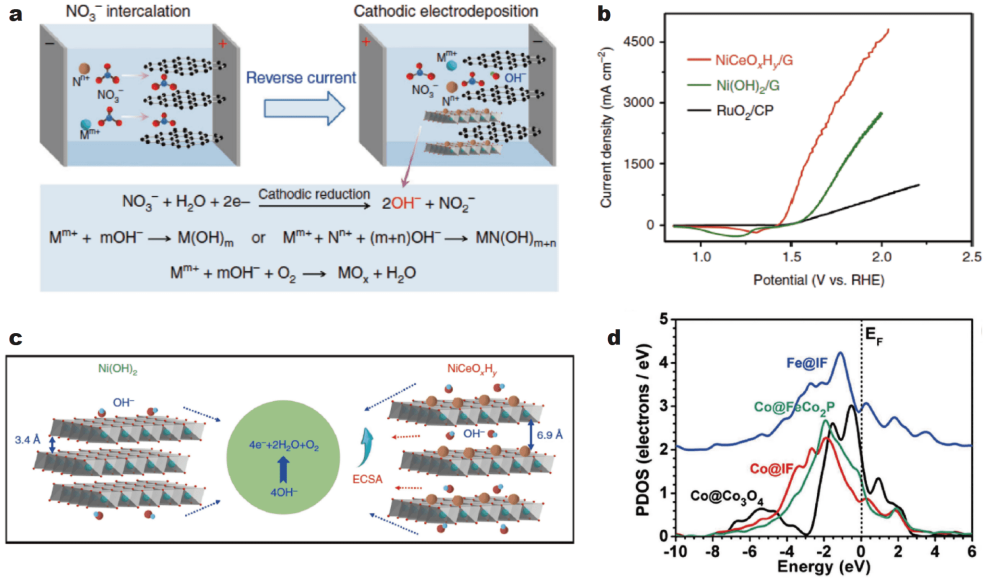

Figure 4 (a) The schematic two-step synthesis and the reaction mechanisms of the cathodic electrodeposition of metal hydroxides ($M(OH)_m$ or $MN(OH)_{m+n}$), and oxides (MO_x). M^{m+} and N^{n+} are metal cations; (b) polarization curves (scan rate 10 mV s^{-1}) of different electrodes; (c) illustration showing that the OER was favored on $NiCeO_xH_y$ with larger interlamellar spacing and higher ECSA compared with $Ni(OH)_2$, respectively. Reprinted with permission [50]. Copyright 2018, Nature Publishing Group. (d) The PDOSs of the Co-3d-bands from different regions within the IF system. Reprinted with permission [51]. Copyright 2018, Wiley.

the CeO_2 in $NiCeO_xH_y$ promoted the formation of γ-NiOOH with larger layer lattices than unmodified $Ni(OH)_2$, which significantly increased the electrochemically active surface area (ECSA), exposed more catalytic sites for OER and enhanced the migration of reactants (Fig. 4c). Moreover, the electronic properties of Ni were modified by Ce, and the DFT calculations revealed that the adsorption properties of the intermediates were also optimized. Zhang *et al.* [51] constructed a $Co_3O_4/Fe_{0.33}Co_{0.66}P$ interface by partially etching $Co(CO_3)_{0.5}(OH)\cdot 0.11H_2O$–Co-CHH nanowire with $Fe(CN)_6^{3-}$ to form the precursor Co-CHH/$FeCo_2(CN)_6$, followed by phosphorization with $NaH_2PO_2\cdot H_2O$ under 350°C. The PDOS results demonstrated that the d-band of Co site on the interface was downshifted (Fig. 4d), which helped to weaken the overbinding effect and facilitate the adsorption/desorption of oxygen species during OER. Moreover, the overlapping effects of O 2p and H 1s orbitals of the intermediates were also optimized. Consequently, the OER energy barrier of each elementary step on $Co_3O_4/Fe_{0.33}Co_{0.66}P$ was significantly lowered and the electron current density was increased. Experimental results proved the DFT results and the $Co_3O_4/Fe_{0.33}Co_{0.66}P$ exhibited a low overpotential of 215 mV at 50 mA cm^{-2}. Yu *et al.* [52] fabricated a series of Ni-Mo-O catalysts for HER and urea oxidation reaction (UOR) *via* annealing $NiMoO_4.xH_2O$ in H_2 and Ar, respectively. The H_2-reduced sample led to the formation of Ni/NiO/MoO_x composite with a synergistic effect: water molecule was firstly dissociated on NiO into hydrogen, which was then stabilized on Ni and finally formed H_2 on MoO_x. On the other hand, the Ar-calcined sample formed $NiMoO_4$ composite, where Mo^{6+} made it easier for Ni^{2+} to be oxidized to Ni^{3+} and promoted the UOR activity. Consequently, the urea electrolyzer composed of Ni/NiO/MoO_x (cathode) and $NiMoO_4$ (anode) exhibited a remarkable low cell voltage of 1.38 V at 10 mA cm^{-2}.

There are also some other studies that combine different strategies to design the composite and structure of catalysts. For example, An *et al.* [53] simultaneously investigated the effect of anion dopant and the interface on HER and OER. A heterogeneous electrocatalyst (N-$NiMoO_4/NiS_2$) was engineered *via* N doping and sulfuration of $NiMoO_4$ nanowires. The PDOS results revealed that the N dopants led to a higher occupation at Fermi level in N-$NiMoO_4$ compared with $NiMoO_4$ (Fig. 5a), which strengthened the adsorption of reaction intermediates. Moreover, the bandgap was also decreased and the charge transfer was therefore facilitated. On the other hand, the electrons were proved to migrate from $NiMoO_4$ to NiS_2 through the heterojunction (Fig. 5b), which contributed to stabilizing the adsorbed H atom and facilitating the HER kinetics. Besides, the reduced electron concentration of $NiMoO_4$ led to a higher valence

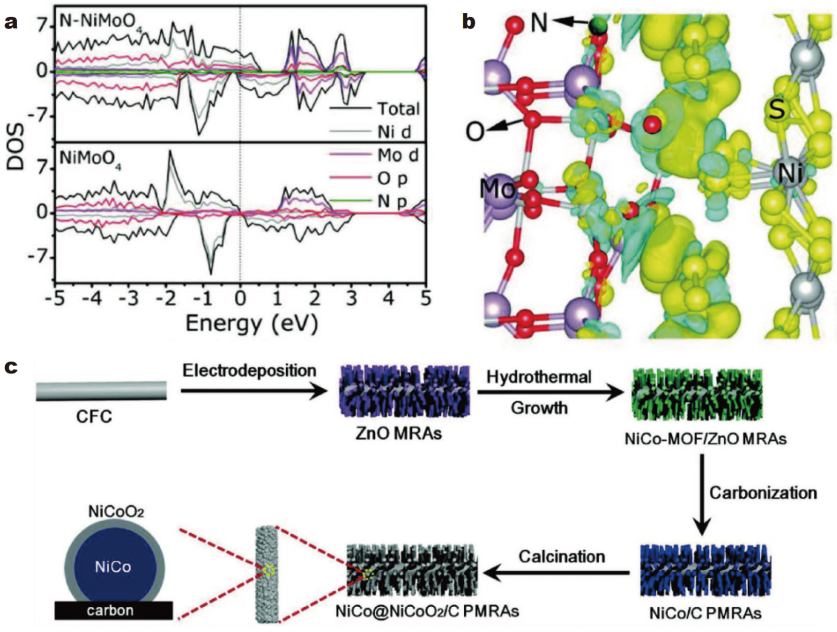

Figure 5 (a) PDOS of different samples; (b) differential charge density of N-$NiMoO_4/NiS_2$ heterojunction. Reprinted with permission [53]. Copyright 2019, Wiley. (c) Process of preparing NiCo@$NiCoO_2$/C PMRAs. Reprinted with permission [54]. Copyright 2018, Wiley.

state of Ni and helped to enhance the OER activity. Finally, the electrolyzer assembled by N-$NiMoO_4$/NiS_2 as both anode and cathode required only 1.6 V to reach 10 mA cm^{-2}. Xu *et al.* [54] fabricated porous microrod arrays composed of carbon-confined NiCo@$NiCoO_2$ core@shell nanoparticles (NiCo@$NiCoO_2$/C PMRAs) through carbonization and calcination of NiCo-MOF/ZnO microrod arrays (Fig. 5c). The microstructures exhibited a high ECSA with abundant catalytic sites for OER, and the charge transfer was facilitated by the surface oxygen vacancies of $NiCoO_2$. Consequently, the electrode of NiCo@$NiCoO_2$/C PMRAs required an overpotential of only 366 mV to reach 20 mA cm^{-2} and exhibited a high stability of 20 h. Duan *et al.* [55] fabricated a series of $ZnCo_{2-x}Ni_xO_4$ (x=0–2) catalysts *via* thermal decomposition of a mixture of $Zn(OAc)_2{\cdot}2H_2O$ and $Co(NO_3)_2{\cdot}6H_2O$ with turnable Zn/Co ratios. *Via* DFT +U calculations, they first found the gap between the O p-band and M_{oh} (Co and Ni) d-band center in the nanomaterial significantly affected the stability. Namely, when $x \leq 0.4$, the energy of O was close to or lower than that of M_{oh}, indicating that the lattice was stable and it was hard to release lattice oxygen. However, when $x \geq 0.6$, the energy of O rapidly increased and therefore the metastable structure with unstable lattice oxygen formed. On the other hand, the lowest unoccupied molecular orbital (LUMO) of the lattice reflected the ability to release lattice oxygen in the spinel and therefore was correlated with the OER activity. The LUMO changed from Ni-substitution demonstrated that 33% Ni-substitution led to the lowest LUMO of the spinel. Therefore the $ZnCo_{1.4}Ni_{0.6}O_4$ and $ZnCo_{1.2}Ni_{0.8}O_4$ would exhibit more active redox and release more lattice oxygen during the reaction. The electrochemical test matched well with the theoretical results. Surface reconstruction was easily induced on both $ZnCo_{1.4}Ni_{0.6}O_4$, and $ZnCo_{1.2}Ni_{0.8}O_4$, and the active phase (NiOOH) was formed after a few cycles. Consequently, the metastable spinel catalysts significantly outperformed other stable spinels. Table 1 summarizes the performances of some representative oxide-based electrocatalysts.

Transition metal sulfides

Transition metal sulfides have shown unique physicochemical properties and a significantly enhanced conductivity compared with metal oxides, which make them promising candidates for many electrochemical applications [56–63]. Due to the higher electronegativity, the S sites in the sulfides can withdraw electrons from the metals and then act as efficient active sites for reactant adsorption and activation [64]. Meanwhile, in alkaline HER, the S sites can promote the water dissociation *via* forming the $S^{\sigma+}$–TM^{n+}–H_2O network. Different strategies have also been developed for the improvement of transition metal sulfides. Exploring highly active facets for electrocatalysis is important for improving the activity. Dong *et al.* [65] prepared a highly porous Ni_3S_2 thin film (Ni_3S_2 NTFs) *via* sulfidation of anodized nickel oxide supported on nickel foils. They successfully prepared Ni_3S_2 NTFs and dominatingly exposed (003) facet consisted of Ni_3-triangle and S atoms. Theoretical calculations demonstrated that the Ni_3S_2 was metallic with high electron conductivity. Meanwhile, the porous structure exposed abundant catalytic sites and enhanced the mass transfer, and the surface exhibited a hydrophilic property that enabled good adsorption of reactants. Moreover, both the water dissociation and the hydrogen adsorption/desorption ability were significantly enhanced on Ni_3S_2

Table 1 Comparison of the performances of transition metal oxide-based electrocatalysts for different applications

Catalyst	Substrate	Electrolyte /reaction	Overpotential (mV)@mA cm^{-2}	Tafel slope (mV $decade^{-1}$)	Stability (mA cm^{-2}@h)
Co_3O_4-NP/N-rGo [41]	Carbon cloth	1 mol L^{-1} KOH/OER	380@10	62	
$CaMnO_3$/S [43]	Carbon paper	0.1 mol L^{-1} KOH/OER	470@10	52	2000 cycles
N-Co_3O_4 [44]	Ni foam	0.1 mol L^{-1} KOH/OER	300@10	36.3	10@1
Ni, Zn dual-doped CoO [45]	Carbon fiber paper	1 mol L^{-1} KOH/HER	53@10		10@24
Co-MnO_2 [46]	Glassy carbon	1 mol L^{-1} KOH/OER	279@10	75	10@12
CoV-UAH [47]	Glassy carbon	1 mol L^{-1} KOH/OER	250@10	44	40@170
$NiCeO_xH_y$ [50]	Glassy carbon	1 mol L^{-1} KOH/OER	177@10	22	1000@300
$Co_3O_4/Fe_{0.33}Co_{0.66}P$ [51]	Ni foam	1 mol L^{-1} KOH/OER	215@50	59.8	240@150
N-$NiMoO_4$/NiS_2 [53]	CFC	1 mol L^{-1} KOH/OER	283@10	44.3	20@29
NiCo@$NiCoO_2$/C [54]	CFC	1 mol L^{-1} KOH/OER	366@20	83.97	20@20

(003) facet with Ni_3-triangle and S atoms (Fig. 6a, b). The electrolyzer using Ni_3S_2 NTFs as electrodes required only 1.611 V to reach 10 mA cm^{-2}.

Tuning the ratio of anion/cation in the material can also induce a varied intrinsic activity. Li *et al.* [66] prepared a-MoS_x (x=2.73) *via* a controllable laser ablation method from the aqueous phase Mo precursor (Fig. 6c). The as-synthesized a-MoS_x maximized the ratio of Mo^V defects compared with MoS_2 or MoS_3, and the number of bridging ligands of S_2^{2-} was also optimized. Theoretical and experimental results demonstrated that the Mo^V defects and bridging S_2^{2-} were excellent HER sites. Meanwhile, the charge resistance was reduced and more active sites were exposed on MoS_x. Therefore, the HER performance of MoS_x was superior to those of other molybdenum sulfides. Yang *et al.* [67] synthesized CoNiFe sulfide nanospheres with numerous mesopores (CoNiFe-S MNs) (Fig. 6d) as a durable electrocatalyst for OER and ORR through a simple two-step solvothermal method. The trimetallic ions in the composite had a cooperative effect on the mesoporous structure and the outstanding catalytic performance. Among trimetallic ions, the incorporation of Fe was employed as an electron donor that provided electrons to Co and Ni to weaken the oxygen adsorption and favor the reaction. In addition, both the mesopores and the synergistic effect of trimetallic ions enlarged the electrochemical double-layer capacitance and exposed more catalytic sites for OER. As a result, the CoNiFe-S MNs exhibited outstanding OER (an overpotential of 199 mV at 10 mA cm^{-2}) and ORR performances (a half wave potential of 0.78 V) with high stability. Kong *et al.* [68] prepared a three-dimensional (3D) hybrid Ni-Mo sulfide material supported by carbon textiles ($NiMo_3S_4$/CTs) using a facile hydrothermal method followed by post-annealing. Owing to the insertion of Ni into the MoS_2 lattice, the interlayer spacing was enlarged and therefore more catalytic sites with abundant defects were formed. Meanwhile, the 3D nanostructure increased the ECSA and facilitated the electron and ion transfer. Besides, the carbon textile also helped to reduce the charge resistance and inhibited the agglomeration of sulfides during the reaction. The $NiMo_3S_4$/CTs showed an efficient HER performance with a high stability.

Engineering heterostructures can also improve the electrocatalytic performance of metal sulfides [69]. Muthurasu *et al.* [70] engineered a Co_3O_4/MoS_2 heterostructure *via* immersing Co_3O_4 in MoS_2-containing dimethyl formamide (DMF) solution followed by a solvothermal process under 200°C, causing a strong interaction between the two compounds. The MoS_2 enhanced the exposure of cobalt sites that acted as the OER active centers. Meanwhile, MoS_2 promoted the adsorption of OER intermediates and therefore facilitated the reaction kinetics. In return, the electron transfer between S and O

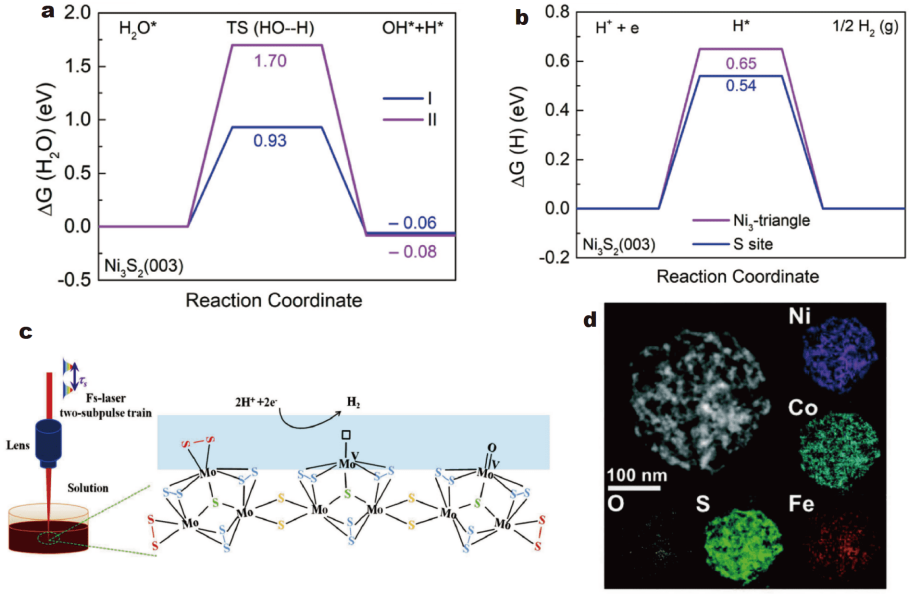

Figure 6 Calculated adsorption free energy diagrams for the (a) Volmer step and (b) Tafel step on the Ni_3S_2(003) facet model. Reprinted with permission [65]. Copyrith 2019, Elsevier. (c) Schematic of the preparation process, structure of a-MoS_x, and HER catalytic mechanism. Reprinted with permission [66]. Copyright 2019, Wiley. (d) High angle annular dark field scanning transmission electron microscope (HAADF-STEM) and elemental mapping images of $NiCo_2S_4$ and $FeNi_2S_4$. Reprinted with permission [67]. Copyright 2018, Wiley.

on the interface promoted the conductivity and induced higher adsorption of proton during HER. Consequently, Co_3O_4/MoS_2 showed good performances for both HER and OER. Liu *et al.* [71] construed an interface between $(Ni,Fe)S_2$ nanoboxes and MoS_2 nanoarrays ($(Ni, Fe)S_2@MoS_2$) (Fig. 7a), which showed an excellent overall water splitting performance. *In-situ* Raman results demonstrated that it was easier for the S edges on the heterostructure to form the $S–H_{ads}$ and the binding strength of intermediates (H^* and OH^{-*}) was optimized, leading to a faster reaction kinetics. Kim *et al.* [72] reported a hierarchically structured Ni_2P/MoS_2 supported by nitrogen-doped carbon for HER. The hierarchical Ni_2P/MoS_2 structure was fabricated *via* direct phosphidation of N-doped carbon-supported $NiMoS_4$ (Fig. 7b). It was proved that the surface Ni_2P induced an activation of the MoS_2 basal planes, which significantly improved the intrinsic HER rate on MoS_2. Moreover, the heterostructure synergistically increased the electron transfer and enlarged the ECSA, which also enhanced the reaction kinetics. The as-prepared nanomaterials exhibited a platinum-like HER activity with good stability in 0.5 mol L^{-1} H_2SO_4. Nguyen *et al.* [73] engineered a $CoS_x@Cu_2MoS_4$-MoS_2/NSG composite *via* refluxing the precursors followed by a two-step calcination with controllable heating rate and gas flow rate, the as-prepared material showed a core-shell heterostructure (Fig. 7c, d), which exhibited numerous advantageous physicochemical properties: (i) the Cu and Mo in Cu_2MoS_4 induced the neighboring S to be effective electrocatalytic active sites, which showed an appropriate oxygen adsorption property and O–O bond cleaving ability. (ii) The sulfur in the crystal helped to induce defects that contributed to forming surface oxyhydroxide for oxygen evolution. (iii) The core-shell structure of

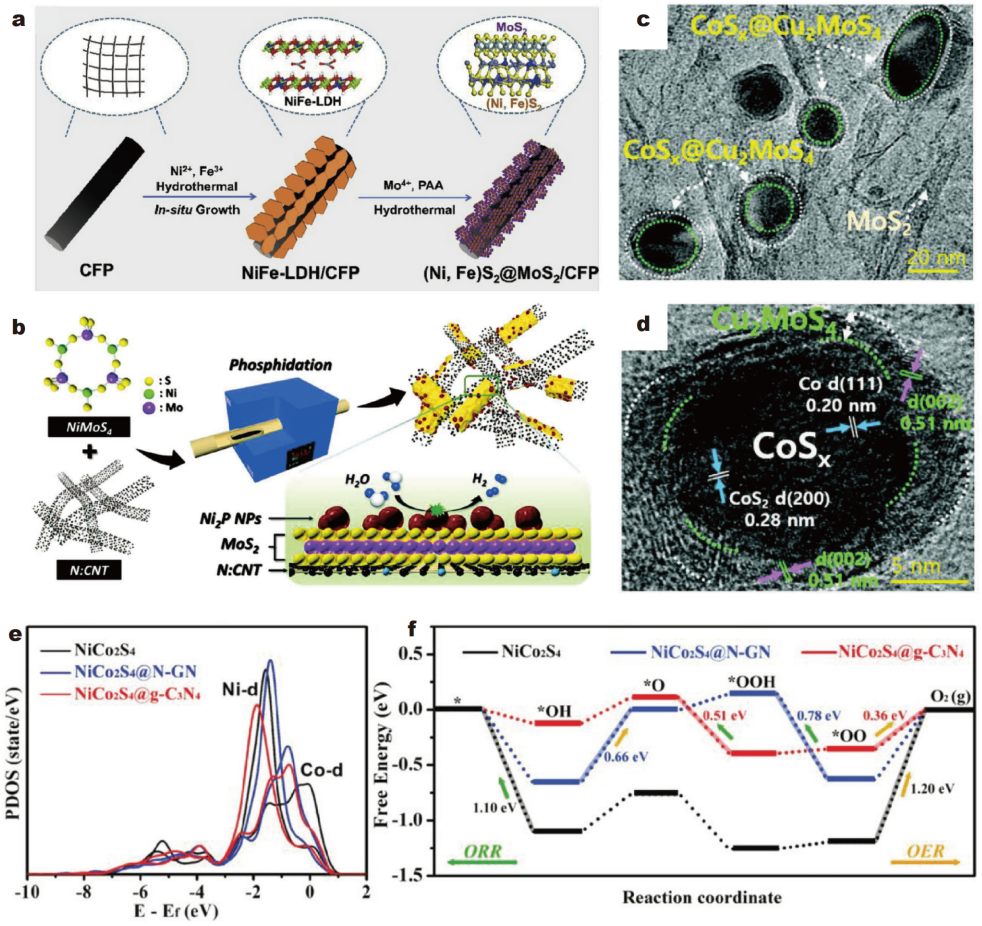

Figure 7 (a) Preparation of $(Ni, Fe)S_2@MoS_2$ heterostructures. Reprinted with permission [71]. Copyright 2019, Elsevier. (b) Fabrication process of Ni_2P anchored on MoS_2 supported on N:CNT. Reprinted with permission [72]. Copyright 2019, Wiley. (c, d) High-resolution TEM (HRTEM) images of the $CoS_x@Cu_2MoS_4$-MoS_2/NSG hybrid. Reprinted with permission [73]. Copyright 2020, Wiley. (e) Calculated d-band positions of metallic Ni and Co sites and (f) free energy diagrams of ORR and OER processes on different samples. Reprinted with permission [74]. Copyright 2019, Wiley.

CoS_x@Cu_2MoS_4 exposed more edge-terminated sites that showed excellent intermediate adsorption/desorption properties. (iv) The electronic state of CoS_x@Cu_2MoS_4 was upshifted to the Fermi level, which strengthened the binding between the active sites and reactants. (v) The high conductivity and ECSA realized a good mass and charge transfer ability. Therefore, CoS_x@Cu_2MoS_4-MoS_2/NSG was simultaneously active in HER, ORR and OER. Moreover, the CoS_x@Cu_2MoS_4-MoS_2/NSG-based Zn-air battery realized a high cell voltage of ca. 1.44 V with a power density of 40 mW cm^{-2} at 58 mA cm^{-2}, which outperformed the commercial Pt/C. Table 2 summarizes the performances of some representative oxide-based electrocatalysts. Han *et al.* [74] prepared a novel $NiCo_2S_4$/graphitic carbon nitride/carbon nanotube ($NiCo_2S_4$@g-C_3N_4-CNT) composite by a two-step hydrothermal approach and a vacuum filtration process. The CNT support provided a porous network structure that facilitated the charge transfer. Experimental studies revealed the electronic interactions between bimetallic Ni/Co active sites and abundant pyridinic-N species in g-C_3N_4. Theoretical calculations demonstrated the unique co-activation of bimetallic Ni/Co atoms by pyridinic-N species *via* downshifting their d-band center positions and therefore benefitting the adsorption/desorption features of oxygen intermediates (Fig. 7e). Consequently, $NiCo_2S_4$@g-C_3N_4-CNT showed a high onset potential of 0.87 V for ORR and surpassed many of the reported TMC-based electrocatalysts (Fig. 7f). Cao *et al.* [75] fabricated a NiS_2/CoS_2 heterostructure as ORR electrocatalyst by an ion hot-injection method. The lattice distortion in the interface induced an electronic modulation, provided abundant electrocatalytic active sites and enhanced the electronic conductivity during the electrochemical process. Consequently, NiS_2/CoS_2 displayed a diffusion current density of 4.87 mA cm^{-2}, much higher than that of NiS_2 and CoS_2. Meanwhile, NiS_2/CoS_2 showed an onset potential of 0.90 V and half-wave potential of 0.79 V, which were comparable to those of commercial Pt/C.

Transition metal selenides

As congeners, transition metal selenides have similar physiochemical properties with sulfides. Moreover, compared with oxides and sulfides, transition metal selenides exhibit a metallic nature with a faster electron transfer ability, which significantly favors the electrochemical reaction process [76–81]. However, their composite and structural properties are still needed to be improved to compete with noble metal-based electrocatalysts. Various carbon supports have been applied to enhance the exposure of active sites and further increase the conductivity [82,83]. Shi *et al.* [84] prepared polycrystalline Ni_3Se_2 arrays on a nickel foam (Ni_3Se_2/NF) using a solvothermal method, and the as-prepared Ni_3Se_2

Table 2 Comparison of the performances of transition metal sulfide-based electrocatalysts for different applications

Catalyst	Substrate	Electrolyte /reaction	Overpotential (mV)@mA cm^{-2}	Tafel slope (mV $decade^{-1}$)	Stability (mA cm^{-2}@h)
MoS-CoS-Zn [58]	Glassy carbon	0.5 mol L^{-1} H_2SO_4/HER	72.6@10	37.6	10@60
Co_9S_8/NSG-8 [61]	Glassy carbon	1.0 mol L^{-1} KOH/OER	260@10	55	2000 cycles
Ni_3S_2 NTFs [65]	Ni foam	1.0 mol L^{-1} NaOH/HER	177@20	75.7	10@30
Ni_3S_2 NTFs [65]	Ni foam	1.0 mol L^{-1} NaOH/OER	319@20	101.2	10@30
a-MoS_x [66]		0.5 mol L^{-1} H_2SO_4/HER	145@10	40	1000 cycles
CoNiFe-S MNs [67]	Carbon fiber paper	1.0 mol L^{-1} KOH/OER	199@10	50.1	1.54 V@50
CoNiFe-S MNs [67]	RRDE	0.1 mol L^{-1} KOH/ORR	$E_{1/2}$=0.78 V		10
$NiMo_3S_4$/CTs [68]	Carbon textiles	0.5 mol L^{-1} H_2SO_4/HER	124@10	46.2	72 h
Co_3O_4/MoS_2 [70]	Ni foam	1.0 mol L^{-1} KOH/OER	230@20	45	20@13
Co_3O_4/MoS_2[70]	Ni foam	1.0 mol L^{-1} KOH/HER	205@10	98	10@14
(Ni, Fe)S_2@MoS_2 [71]	Carbon fiber paper	1.0 mol L^{-1} KOH/HER	130@10	101.22	10@44
(Ni, Fe)S_2@MoS_2 [71]	Carbon fiber paper	1.0 mol L^{-1} KOH/OER	270@10	43.21	1.52–1.55 V@44
Ni_2P/MoS_2/N:CNT [72]	Glassy carbon	0.5 mol L^{-1} H_2SO_4/HER	93.9@10	57.8	3000 cycles
CoS_x@Cu_2MoS_4-MoS_2/NSG [73]	Carbon paper	0.1 mol L^{-1} KOH/HER	118.1@10	41.1	10@33
CoS_x@Cu_2MoS_4-MoS_2/NSG [73]	Carbon paper	0.1 mol L^{-1} KOH/OER	351.4@10	61.5	10@33
CoS_x@Cu_2MoS_4-MoS_2/NSG [73]	RRDE	0.1 mol L^{-1} KOH/ORR	$E_{1/2}$=0.89 V	53.5	16.4 h

RRDE: rotating ring-disk electrode.

nanowires exposed abundant gain boundaries on the surface. The gain boundaries and the surface-rough nanowire morphology of the selenides provided abundant catalytic sites during reactions. Moreover, the adsorption and transport properties of reactants were significantly enhanced owing to the structural properties. The Ni_3Se_2/NF showed efficient overall water splitting performance. Wang *et al.* [85] prepared coral-like $NiSe_2$/g-C_3N_4 hybride using a hydrothermal method, where the $NiSe_2$ particles were uniformly affixed on the layers of graphitic carbon nitride. The structural properties contributed to facilitating the charge transfer and enhancing the intrinsic activity of $NiSe_2$. The material showed efficient OER activity (an overpotential of 290 mV at 40 mA cm^{-2}). Wang *et al.* [86] reported a CS@CNC NAs/CC nanomaterial using a co-precipitation method followed by selenylation in inert atmosphere (Fig. 8a). Owing to the carbon framework, the $CoSe_2$ nanoparticles were confined in the cobalt-nitrogen-doped carbon layers with good dispersion. The framework not only enabled fast charge and mass transfer, but also helped to expose more active sites for the reaction. Meanwhile, the adsorption properties of the intermediates on $CoSe_2$ were also optimized, and the agglomeration of $CoSe_2$ was inhibited. As a result, the CS@CNC NAs/CC required only 84 mV to reach 10 mA cm^{-2} with a 72-h stability.

Tuning the phase of selenides from 2H to 1T can significantly increase the conductivity and expose more active sites [87]. Deng *et al.* [88] first loaded $MoSe_2$ NSs onto a nitrogen-doped porous carbon support and then intercalated PO_4^{3-} into the 2H $MoSe_2$, which finally formed a carbon-supported bi-phase-coexisting $MoSe_2$ hybrid ((1T-2H)-$MoSe_2$/N-MSC). The highly conductive N-MSC support greatly reduced the charge resistance and the 2D morphology of 1T $MoSe_2$ increased the exposed active sites. Meanwhile, the decreased bandgap of 1T $MoSe_2$ led to a higher conductivity (Fig. 8b, c). Moreover, the DFT calculations demonstrated a reduced HER energy barrier and favorable hydrogen desorption of hydrogen on the bi-phase-$MoSe_2$ (Fig. 8d). Benefiting from these unique advantages, the P-$MoSe_2$/N-MSC exhibited a high HER activity (−126 mV at 10 mA cm^{-2}) with high durability. Deng *et al.* [89] first prepared TiC-C arrays *via* a facile CVD method, and then they loaded 1T-$MoSe_2$ NSs onto TiC-C *via* a hydrothermal method. After Ar thermal treatment and NH_3 annealing, a nitrogen-doped $MoSe_2$/TiC-C hierachical material with phase and morphology modulation was fabricated. From the results of theoretical calculation, the incorporation of nitrogen not only led to a narrow band gap of the pristine molybdenum selenide, but also induced a phase transformation from 2H to 1T $MoSe_2$. The DFT calculations revealed that the N-doped $MoSe_2$ exhibited a lower energy for H_2 formation and higher ability for H_2 desorption compared with 1T and 2H $MoSe_2$. Besides, the highly conductive TiC-C substrate significantly reduced the charge transfer resistance and increased the exposure of catalytic sites, which further promoted the reaction kinetics. The $MoSe_2$/

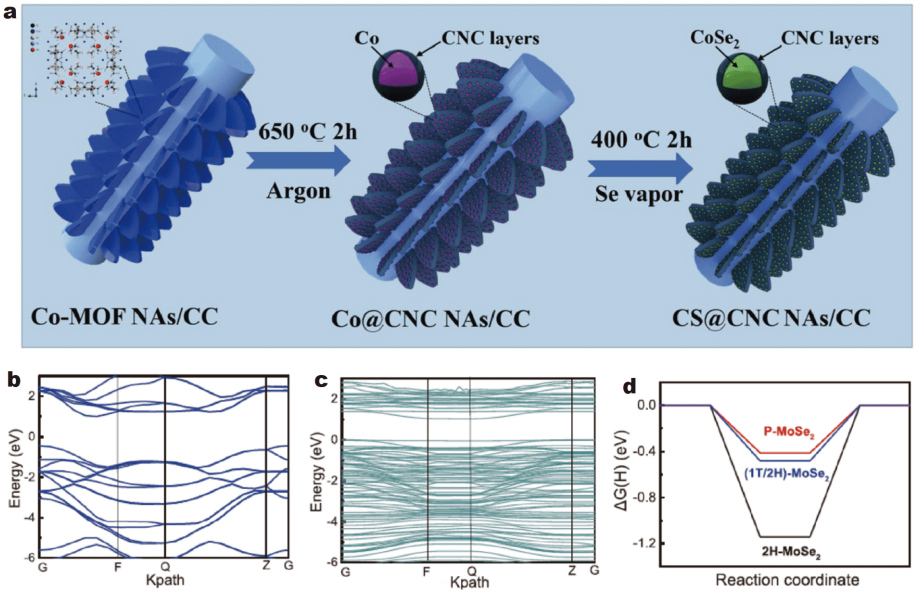

Figure 8 (a) Fabrication process of CS@CNC NAs/CC. Reprinted with permission [86]. Copyright 2019, Elsevier. (b, c) Calculated band structures of 2H-$MoSe_2$ and P-$MoSe_2$, respectively, (d) HER free energy diagrams of different selenides. Reprinted with permission [88]. Copyright 2019, Wiley.

Table 3 Comparison of the performances of transition metal selenide-based electrocatalysts for different applications

Catalyst	Substrate	Electrolyte /reaction	Overpotential (mV)@mA cm^{-2}	Tafel slope (mV $decade^{-1}$)	Stability (mA cm^{-2}@h)
$CoSe_2^{(400)}$-NC-800 [76]	Glassy carbon	1.0 mol L^{-1} KOH/HER	234@10	95	45@13.8
Meso-CoSSe-12h [77]	Glassy carbon	0.5 mol L^{-1} H_2SO_4/HER	110@10	52	100@25
Fe7.4%-NiSe [79]	Ni foam	1.0 mol L^{-1} KOH/OER	231@50	43	0.217 V@22
$SnSe_2$/GNS [81]	Graphite NSs	0.5 mol L^{-1} H_2SO_4/HER	382@10	109.3	5000 cycles
Ni_3Se_2/NF [84]	Ni foam	1.0 mol L^{-1} KOH/OER	320@100	58	6000 cycles
Ni_3Se_2/NF [84]	Ni foam	1.0 mol L^{-1} KOH/HER	95@50	67	6000 cycles
$NiSe_2$/g-C_3N_4 [85]	Ni foam	1.0 mol L^{-1} KOH/OER	290@40	143	1.42 V@10
CS@CNC NAs/CC [86]	Carbon cloth	0.5 mol L^{-1} H_2SO_4/HER	84@10	38	2000 cycles
P-$MoSe_2$/N-MSC [88]	Carbon cloth	0.5 mol L^{-1} H_2SO_4/HER	126@10	51	10@10
N-$MoSe_2$/TiC-C [89]	TiC-C	0.5 mol L^{-1} H_2SO_4/HER	106@10	32	100@4
Co-Se1 [92]	Co foil	1.0 mol L^{-1} KOH/OER	280@100	40.4	2000 cycles
Co-Se4 [92]	Co foil	1.0 mol L^{-1} KOH/HER	268@100	61.4	2000 cycles

TiC-C exhibited an excellent HER performance (137 mV at 100 mA cm^{-2}) in 0.5 mol L^{-1} H_2SO_4. Zhang *et al.* [90] loaded 1T-$MoSe_2$ NSs onto the NiSe substrates using a hydrothermal method, which formed a 3D core-shell heterostructure with numerous metallic 1T-$MoSe_2$ on the surface (1T-$MoSe_2$/NiSe). During the preparation, the electron transfered from NiSe to $MoSe_2$, inducing the transformation of $MoSe_2$ from 2H- to 1T-phase. The edges of 1T-$MoSe_2$ were highly active sites for HER and the substrate NiSe helped to facilitate the water dissociation. Meanwhile, the 3D conductive heterostructure exposed more catalytic sites, and the charge and mass transfer were facilitated during the reaction. Moreover, the strong interaction between the two selenides contributed to maintaining the 1T-phase of $MoSe_2$. As a result, the 1T-$MoSe_2$/NiSe showed high HER activity with high stability.

In addition, constructing heterostructure and doping are also applied for synthesizing novel selenides [91]. Zhao *et al.* [92] synthesized a 3D cobalt selenide electrocatalyst composed of CoSe and Co_9Se_8 *via* a facile one-step selenization of Co foil with Se powder in a vacuum-sealed ampoule. By manipulating the ratio of Co/Se in the precursor, the electronic state of Co species in the products was regulated and the application of the catalyst would go from OER to HER. The higher charge-stated Co sites promoted the OER kinetics, which was attributed to the easier adsorption and conversion of OH^- with the presence of more high-valent cobalt. Meanwhile, the less $Se^{\delta-}$ sites on the surface could also favor the OER kinetics. While the HER process preferred the lower charge state of Co species, which could be beneficial to the enhanced electron transfer and more exposed active sites. Moreover, the high ratio of surface $Se^{\delta-}$ facilitated the adsorption/desorption of proton and therefore facilitated HER. Yuan *et al.* [93] fabricated a CoSe/$MoSe_2$ nanomaterial using the pyrolysis and selenylation of Mo, Co-based MOFs, which were composed of CoSe nanoparticles and $MoSe_2$ nanolamellas. The strong interaction between CoSe and $MoSe_2$ facilitated the electron transfer and upshifted the d-band center of the selenides, and therefore the adsorption of reactants (OH^-) was reduced. Meanwhile, more defects were formed due to the heterostructure and provided more adsorption sites for OH^-. Besides, the well dispersed nano-sized selenides provided more OER sites. Therefore, the CoSe/$MoSe_2$ required an overpoetntial of only 262 mV to reach 10 mA cm^{-2} with 20-h stability. Jing *et al.* [94] prepared a Fe_3Se_4/FeSe/NPGC heterostructure *via* a simple one-pot reduction method (carbonizing the cornstalk cores immersed by Fe and Se precursors under N_2 protection). The hybride exhibited a porous nanostructure with numerous channels, which significantly promoted the oxygen diffusion and exposed more catalytic sites. The heterojunctions and the carbon support enabled a high charge transfer rate during the reaction. Moreover, the well dispersed selenides and the N-dpoed carbon defects acted as active ORR sites. The Fe_3Se_4/FeSe/NPGCs exhibited efficient ORR performances in 50 mmol L^{-1} PBS electrolyte. Wang *et al.* [95] prepared spinel $CoIn_2Se_4$ NSs, where Co^{2+} occupied the tetrahedral and In^{3+} occupied the octahedral site of the crystal structure *via* fast selenylation of In and

Co precursors by hot-injection of cation solution into anion (Se) solution. The $CoIn_2Se_4$ NSs featured abundant active sites and ideal charge transfer ability for boosting the reaction kinetics. Moreover, the DFT calculations confirmed that the reaction pathway on the surface of spinel selenide can be significantly facilitated. As a result, the $CoIn_2Se_4$ catalyst showed a remarkable ORR performance in the alkaline electrolyte. Moreover, the flexible zinc-air battery using $CoIn_2Se_4$ as the air cathode showed a high open-circuit voltage of 1.37 V, a large specific capacity of 733 mA hg_{Zn}^{-1}, and an energy density of 931 W h kg^{-1}.

Transition metal phosphides

Transition metal phosphides have been widely explored due to their low cost and impressive HER performances, owing to the electronic features of P that can extract electrons from the neighboring metals [24]. As a result, the P sites prefer to attract the protons in the electrolyte, contributing to a suitable bonding between the catalytic sites and the intermediates/products. In addition, researches about phosphides for electrocatalytic oxygen reactions have been also reported recently, extending the applications of phosphides in energy conversion [96–100]. Tuning the crystal structure *via* the strain effect has been proved to be an effective way to improve the activity. Li *et al.* [101] proposed an iron phosphide material modified by carbon for OER, where the carbon induced a tensile strain in FeP_2 crystal during the preparation (Fig. 9a, b). The strain effect of FeP_2 led to an electron redistribution in the hydroxyl when adsorbed on the catalytic site, which led to strengthened adsorption of the intermediates during the reaction. The DFT calculations demonstrated that the energy barrier of the rate-determining step was reduced owing to the carbon-covered strained FeP_2 crystal. Meanwhile, the incorporation of carbon improved the chemical stability of FeP_2 nanoparticles and reduced the charge transfer resistance. Therefore, the catalyst showed an outstanding OER performance.

Dopants can also alter the adsorption properties of the intermediates on phosphides [102]. Cao *et al.* [103] fabricated a N-doped carbon-covered Ni-Co phosphide material supported on nickel foam ($Ni_xCo_{2-x}P$@NC NA/NF). They first fabricated a series of Ni–Co layered hydroxides on Ni foam through a hydrothermal process,

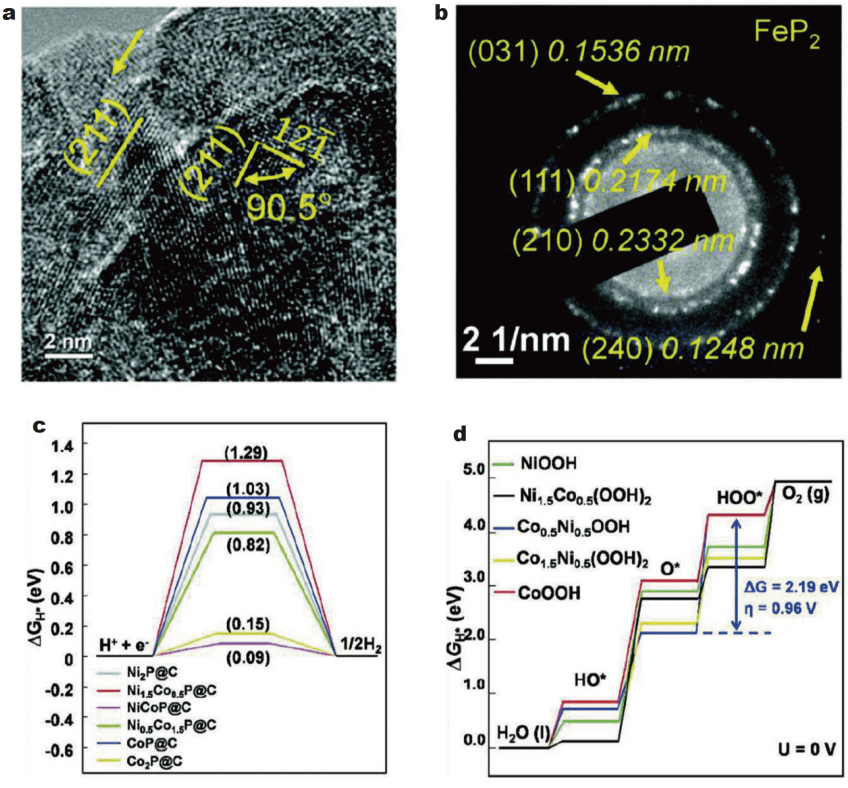

Figure 9 (a, b) HRTEM and the corresponding SAED pattern of FeP_2. Reprinted with permission [101]. Copyright 2020, Wiley. (c) HER free energy diagram of different catalysts, (d) OER free energy diagrams of different catalysts under 0 V. Reprinted with permission [103]. Copyright 2019, Wiley.

and then a phosphidation treatment under N_2 was carried out to form various NixCo$_{2-x}$P nanostructures embedded in N-doped carbon matrix ($Ni_xCo_{2-x}P$@NC NA/NF). *Via* tuning the molar ratio of Ni/Co salts, both the phase and morphology of $Ni_xCo_{2-x}P$ were tuned and embedded in carbon matrix. The designed 3D morphology of the hybrid material not only provided a stable structure, but also improved the electron/mass transfer capability. Moreover, the unique nanostructure of the material enlarged the ECSA, leading to increased exposure of reaction active sites. The DFT calculations revealed that both the Ni/Co ratio and surface played critical roles in determining the reaction energy barrier: for HER, the ΔG_{H^*} on NiCoP@C with a carbon shell on NiCoP was close to zero and therefore suitable for HER (Fig. 9c). For OER, the surface metal oxyhydroxides were responsible for the reaction activity, and the energy barrier of the rate-determining step (formation of O^*) on $Ni_{0.5}Co_{0.5}OOH$ was the lowest among different phosphides, which facilitated the OER kinetics (Fig. 9d). Therefore, the $Ni_{0.5}Co_{0.5}P$@NC NA/NF required only 1.56 V to reach 20 mA cm^{-2} for water splitting. Lv *et al.* [104] used graphene oxide to control the crystal growth and synthesized a hybrid 2D ultrathin Ni-Co phosphide with high porosity (Fig. 10a–c). NiCo(OH)$_x$ was firstly loaded onto graphene oxide and NiCoP NSs were obtained after the calcination and phosphorization. In the NiCoP, electrons migrated from metal ions to P, leading to a higher valance state of Co and Ni, which favored the formation of surface NiOOH or CoOOH for OER. Meanwhile, the P atoms with higher electron density showed a high proton-capture ability during the reaction process. The DFT calculations demonstrated that the energy barriers of both HER and OER were significantly lowered on the one-layer NiCoP than the bulk NiCoP, and the ultrathin NiCoP exhibited a metallic property with high carrier density. Besides, the 2D and porous structure provided more active site for the reaction. The NiCoP NSs required only 34.3 and 245.0 mV to reach 10 mA cm^{-2} for HER and OER, respectively. Wu *et al.* [105] designed N-doped carbon nanotube (NCNT)-wrapped Cr-doped FeNi-P nanomaterial (Cr-doped FeNi-P/NCNT) for HER and OER using a one-step annealing method. Among all compositions, both the NCNT and Cr dopant contributed to lowering the electron transfer resistance. Besides, the NCNT matrix helped to maintain the stability, and the introduction of Cr increased the exposure of catalytic sites. According to the DFT calculations, the Cr doping enhanced the adsorption of H_2O and OH^- and desorption of H_2, which promoted the HER pathway (Fig. 10d). As for OER, the rate-determining step changed from the formation of OOH^* to the formation of O_2 with lower energy barrier after Cr doping, and the theoretical potential also decreased (Fig. 10e). The as-prepared Cr-doped FeNi-P/NCN showed excellent performances for both OER and HER.

Hybrid materials have been proved to show an enhanced activity owing to the synergetic effect [106]. Yu *et*

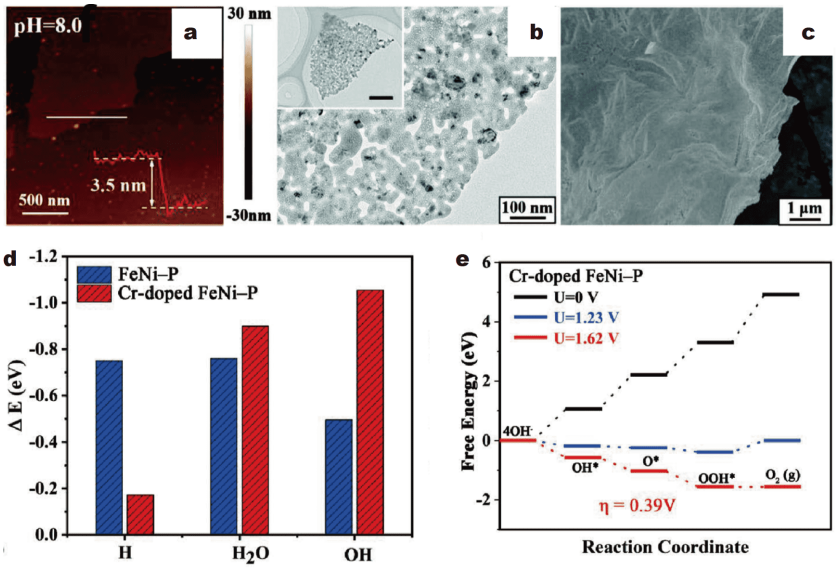

Figure 10 (a–c) AFM image, low-magnification TEM images and SEM image of ultrathin NiCoP NSs. Reprinted with permission [104]. Copyright 2020, Wiley. (d) Adsorption energies of different intermediates on different phosphides, (e) OER free energy profiles of different phosphides. Reprinted with permission [105]. Copyright 2019, Wiley.

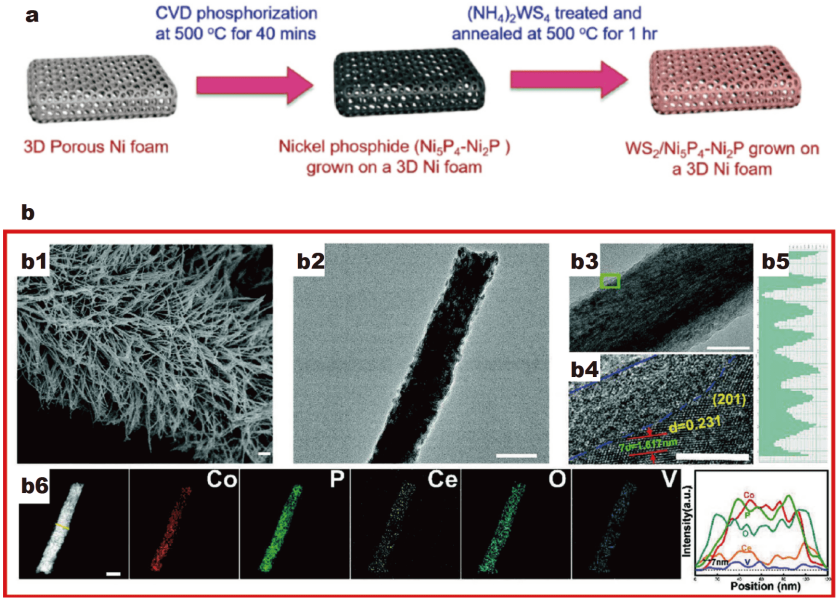

Figure 11 (a) Fabrication of WS_2/Ni_5P_4-Ni_2P hybrid on Ni foam. Reprinted with permission [107]. Copyright 2019, Elsevier. (b) Morphology and element distribution of V-CoP@a-CeO_2. Scale bars in (b1), (b2), (b3), (b4) and (b6), are 1 μm, 100 nm, 50 nm, 5 nm and 100 nm, respectively. Reprinted with permission [108]. Copyright 2020, Wiley.

al. [107] developed the hybridized WS_2/Ni_5P_4-Ni_2P as HER electrocatalysts through a thermal process (Fig. 11a). $WS_{2(1-x)}P_{2x}$ was detected on the surface of the WS_2/Ni_5P_4-Ni_2P, leading to the electron density variation. The combination of WS_2 and Ni_5P_4-Ni_2P effectively increased the ECSA and the active sites for HER, and the electron transportation from Ni_5P_4-Ni_2P to WS_2 enhanced the electrochemical reaction activity. According to the DFT calculation, the new active sites arose with the P and Ni doping into the WS_2. The calculated Fermi levels of NiP_2, Ni_5P_4 and WS_2 were −4.661, −4.953 and −5.462 eV, respectively, which implied the electrons flowed from Ni_5P_4-Ni_2P to WS_2 and facilitated the HER. Yang *et al.* [108] reported a hierarchical vanadium-cobalt phosphide material covered by amorphous cerium oxide (V-CoP@a-CeO_2), which was supported by carbon cloth for HER and OER (Fig. 11b). The material was prepared through a three-step procedure, including the hydrothermal process, phosphorization, and final electrodeposition. Theoretical calculations demonstrated that there was a synergistic effect between V and CeO_2, which altered the electron redistribution in the material and increased the electron density of Co sites. As a result, the hydrogen adsorption on Co sites was optimized and the reaction energy barrier was reduced. Besides, the Co sites with lower valance state favored the formation of surface CoOOH, which was the actual OER site. Moreover, the charge resistance was sharply decreased after the combination of the hybrid metal phosphide and the amorphous ceria, leading to an enhanced electron transfer during the reaction process. The V-CoP@a-CeO_2 only needed a voltage of 1.56 V to reach 10 mA cm^{-2}. Boppella *et al.* [109] prepared a nitrogen-doped carbon-supported 2D CoP/NiCoP composite material using the combination of co-precipitation, electrostatic self-assembly, and phosphorization. The synergy between the two metal phosphide components led to an altered electron distribution, which reduced the energy barrier and facilitated the reaction kinetics. The interface between CoP and NiCoP created more adsorption sites for the reactants. The heterostructure and the 2D morphology of the nanomaterial helped to expose more catalytic sites. The strong coupling between the metal phosphides and the carbon support helped to reduce the electron transfer resistance. Therefore, the CoP/NiCoP composite exhibited an efficient HER performances in a wide pH range. Zhang *et al.* [110] developed a CoP NS combined with CNTs (CoP NS/CNTs) for HER using a hydrothermal synthesis. The CNT support inhibited the agglomeration of CoP and therefore more active sites were exposed. Meanwhile, owing to the strong interaction between CoP and CNTs, the charge-transfer capability of CoP NS/CNTs was significantly enhanced, leading to a more rapid kinetics for HER. Besides, the CNTs favored the wettability of CoP NS and improved the interaction between the active site and water molecule, which significantly promoted the

water dissociation. With all enhanced properties mentioned above, the CoP NS/CNTs only required an overpotential of 68 mV to reach 10 mA cm^{-2}. Table 4 summarizes the performances of some representative oxide-based electrocatalysts.

Transition metal carbides and nitrides

Carbides

Owing to the s- and p-orbitals of neighboring C atoms, the d orbitals of metals in transition metal carbides are broadened and exhibit a Pt-like d band center, making the carbides show noble-metal-like physiochemical properties. As a result, carbides have been regarded as excellent HER electrocatalysts due to their metallic electronic structures, high conductivity, and earth abundance [111–116]. Tuning the phase and engineering the mesostructure can significantly enhance the activity. Baek *et al.* [117] constructed a metastable α-MoC_{1-x} with highly ordered mesopores (MMC) from a nanocasting strategy using silica as the hard template. The DFT calculation showed that the α-MoC_{1-x} had a stronger affinity to OH^* species and could favor the water dissociation during HER compared with hexagonal β-Mo_2C (Fig. 12a). Besides, the unique mesoporous morphology of MMC provided a higher surface area and abundant active sites for HER. Due to the facilitated water dissociation and effective proton transfer of MMC, the Pt/MMC electrocatalyst exhibited high HER performance, which was superior to commercial Pt/C (Fig. 12b). Dopants can also optimize the adsorption of intermediates of carbides. Han *et al.* [118] doped nitrogen into WC nanoarrays on carbon fiber paper *via* a CVD process using WO_3 nanoarrays as the substrate and melamine as the nitrogen source. Theoretical calculations demonstrated that the N dopants downshifted the density of 5d states of W in N-WC compared with that of WC. As a result, the affinity between H and catalytic sites became weaker, which led to an enhanced intrinsic activity. In addition, the morphology of the catalyst not only enlarged the exposure of active sites, but also accelerated the gas releasing. As a result, the as-prepared catalyst only required 190 mV to reach 200 mA cm^{-2}. Karuppannan *et al.* [119] fabricated a nitrogen and fluorine-doped carbon-encapsulated Fe/Fe_3C (NFC@Fe/Fe_3C) electrocatalyst by the carbonization and acid etching of a Fe-poly(aniline-fluoroaniline) copolymer, in which the carbide sites synergistically interacted with F- and N-doped carbon and promoted the adsorption and reduction of oxygen on the ORR catalytic sites. Electrochemical tests showed that NFC@Fe/Fe_3C-9 exhibited a higher $E_{1/2}$ value than commercial Pt/C with an excellent durability in alkaline electrolyte. Moreover, NFC@Fe/Fe_3C-9 exhibited high methanol tolerance in both acidic and alkaline electrolytes.

Constructing hybrids with heterostructures can facilitate the reactions of carbides [120]. Lu *et al.* [121] syn-

Table 4 Comparison of the performances of transition metal phosphide-based electrocatalysts for different applications

Catalyst	Substrate	Electrolyte /reaction	Overpotential (mV)@mA cm^{-2}	Tafel slope (mV $decade^{-1}$)	Stability (mA cm^{-2}@h)
CoP-Doped MOF [97]	Carbon Fiber paper	1.0 mol L^{-1} KOH/HER	34@10	56	2000 cycles
MoP@NCHSs-900 [98]	GCE	1.0 mol L^{-1} KOH/HER	92@10	62	5000 cycles
Ni_2P nanoarray [99]	Ni foam	1.0 mol L^{-1} KOH/HER	306@1000	76	5000 cycles
$NiPS_3$/Ni_2P NSs [100]	GCE	1.0 mol L^{-1} KOH/HER	85@10	82	10@12
Strained FeP_2 [101]	Ni foam	1.0 mol L^{-1} KOH/OER	240@10	56	
NiCoP@NC NA/NF [103]	Ni foam	1.0 mol L^{-1} KOH/OER	305@50	70.5	10@15
NiCoP@NC NA/NF [103]	Ni foam	1.0 mol L^{-1} KOH/HER	37@10	53.9	35@22
Ultrathin NiCoP NSs [104]	Ni foam	1.0 mol L^{-1} KOH/OER	245@10	59.2	5000 cycles
Ultrathin NiCoP NSs [104]	Ni foam	1.0 mol L^{-1} KOH/HER	34.3@10	49.9	5000 cycles
Cr-doped FeNi-P/NCN [105]	Glassy carbon	1.0 mol L^{-1} KOH/OER	240@10	72.36	1000 cycles
Cr-doped FeNi-P/NCN [105]	Glassy carbon	1.0 mol L^{-1} KOH/HER	190@10	68.51	1000 cycles
WS_2/Ni_5P_4-Ni_2P [107]	Ni foam	0.5 mol L^{-1} H_2SO_4/HER	94@10	74	1000 cycles
V-CoP@a-CeO_2 [108]	Carbon cloth	1.0 mol L^{-1} KOH/OER	225@10	58	20@40
V-CoP@a-CeO_2 [108]	Carbon cloth	1.0 mol L^{-1} KOH/HER	68@10	48.1	20@60
CoP NS/CNTs [110]	GCE	1.0 mol L^{-1} KOH/HER	68@10	57	10@24

GCE: glassy carbon electrode.

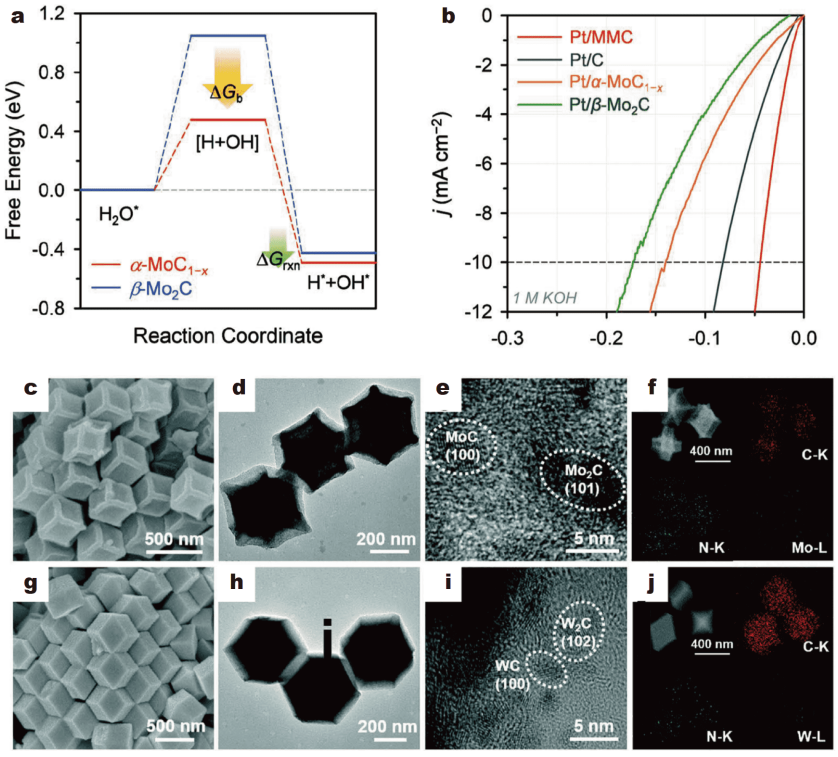

Figure 12 (a) Free energy profiles of water dissociation on different carbides, (b) HER LSV curves of different catalysts. Reprinted with permission [117]. Copyright 2019, Wiley. Field emission scanning electron microscopy (FESEM), TEM, HRTEM images and elemental mapping of (c–f) MoC-Mo_2C/PNCDs and (g–j) WC-W_2C/PNCDs. Reprinted with permission [121]. Copyright 2019, Wiley.

thesized well-dispersed carbide nanocrystals trapped in porous N-doped carbon dodecahedra (MC-M_2C/PNCDs) for HER *via* pyrolysis of Mo/W contained ZIF-8. The TEM images showed that the porous carbon frameworks enfolded the ultrafine carbide nanocrystals with a mixed phase of MC and M_2C (Fig. 12c–j). Owing to the unique compositions and morphology, the catalysts exhibited much higher ESCAs and more active sites than the single-phase carbide, which was beneficial to the diffusion of the electrolyte. And the strong coupling between N-doped carbon and carbides facilitated the electron transfer. Besides, the interaction between MC and M_2C favored the reaction pathways by optimizing the adsorption for reactants. As a result, both MoC-Mo_2C/PNCDs and WC-W_2C/PNCDs exhibited enhanced HER activity compared with single-phased carbides. Li *et al.* [122] developed a metal-organic coordination precursor-assisted strategy for synthesizing porous molybdenum-contained carbon nanomaterials (mC-Mo). Dopamine hydrochloride was applied to induce the self-assembly of Mo-based nanocrystalline and silica was chosen as the hard template. The Mo_2C and Mo_2N nanocrystallines were well confined in the as-prepared mesoporous materials, which showed a much higher surface area compared with nonmesoporous materials. Due to the mesoporous structure, the exposed active sites were significantly increased, which led to stronger mass and charge transfer properties. Besides, the interaction between Mo_2C and Mo_2N induced a synergistic effect and provided a novel $Mo^{\sigma+}$ site, which was highly active for HER. The mC-Mo electrocatalyst outperformed commercial Pt/C in alkaline HER at high current densities. Li *et al.* [123] synthesized novel N-doped carbon nanofibers that contained Ni and Mo_2C nanoparticles (Ni/Mo_2C-NCNFs) *via* a facile electrospinning method combined with a post-synthesis carbonization. Combining the electrospinning and carbonization process, the Ni and Mo_2C nanocrystallines were well dispersed and strongly coupled in the carbon framework. Owing to the structural and composite properties, the electron/mass transfer capability and the exposure of active sites were favored. Moreover, the strong coupling between Ni and Mo_2C induced electron transfer from Ni to Mo_2C. As a result, the adsorption of H on Ni and Mo_2C was simultaneously optimized during HER, and the water dissociation at Ni sites was also favored. On the other hand, the metal-carbide interaction

induced an upshifted Ni d-band center and therefore the affinity between OH^- and Ni was enhanced during OER. The Ni/Mo_2C-NCNFs showed a high overall water splitting performance (a cell voltage of 1.64 V to reach 10 mA cm^{-2}).

Nitrides

Transition metal nitrides are novel metallic electrocatalysts with unique physiochemical and electronic properties [124–128]. Owing to the neighboring N atoms, the d-electron density of metals is increased and the contraction of the d-band center occurs, which induces that the nitrides show a similar electronic structure with Pt-group metals [124]. In addition, nitrides show high electron transfer ability and stability during the reaction [24]. Panda *et al.* [129] synthesized cubical CuN_3 by the nitridation of copper acetate, which efficiently catalyzed HER, OER, and overall water splitting. Notably, water molecules could easily attack the coordinatively unsaturated copper sites in CuN_3 and be deprotonated, which induced the formation of oxo-bridged copper sites and a CuO shell. Additionally, lots of vacancies and CuO (H) structure with defects were generated through oxidative potentials (Fig. 13a, b). The strong collaborative effect between the amorphous overlayer and CuN_3 and the defected structure helped to optimize the adsorption of the intermediates during OER. And metallic Cu-enriched CuO surface favored the HER pathways. Consequently, the electrolyzer assembled by CuN_3 showed a voltage of 1.62 V at 10 mA cm^{-2} with 10-day stability. The carbon support can alter the adsorption of the intermediates on nitrides. Miao *et al.* [130] prepared an h-MoN/BCNT nanomaterial, where hexagonal MoN nanoparticles were well encapsulated in B,N-codoped CNTs (BNCNTs) (Fig. 13c, d). They postmodified the Mo-based polyoxometalates, which were reduced by hexamethylenetetramine (HMT) with ammonia gas in the BNCNT. A large number of MoN NSs spread over the nanotubes (BNCNTs), which helped to expose abundant active sites and enhanced the electron transfer. The DFT calculations

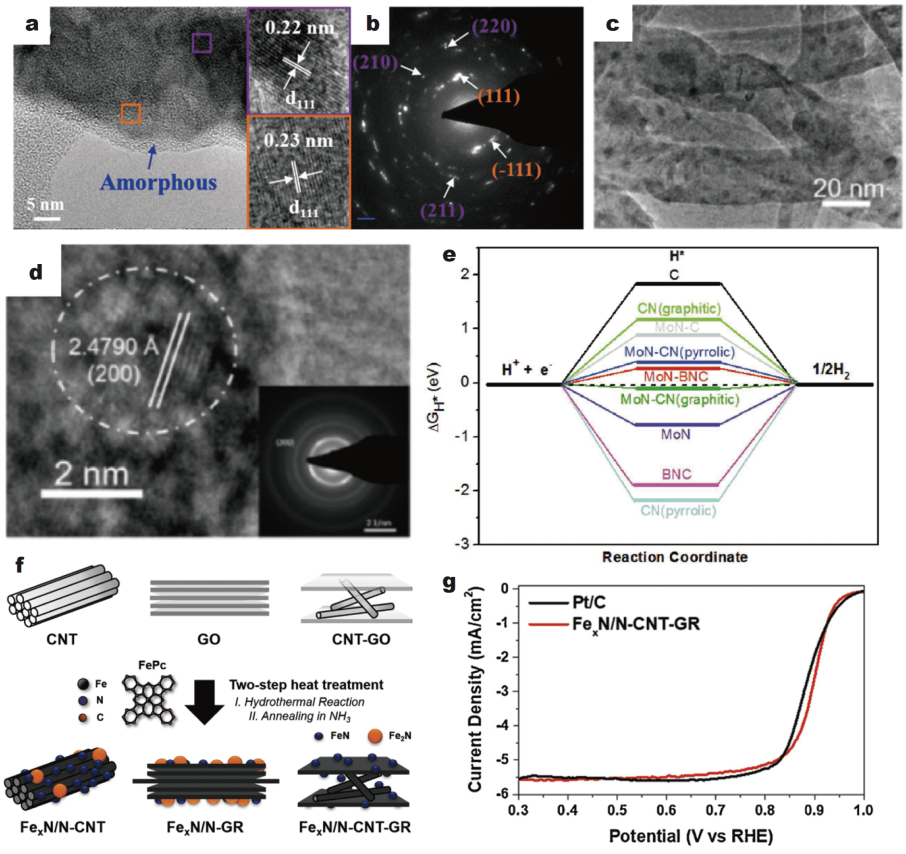

Figure 13 (a) HRTEM images and (b) SAED pattern of Cu_3N post-OER. Reprinted with permission [129]. Copyright 2019, American Chemical Society. (c, d) TEM and HRTEM images of h-MoN@BNCNT, (e) free energy of hydrogen adsorption on different samples. Reprinted with permission [130]. Copyright 2019, Wiley. (f) Schematic illustration of preparation of Fe_xN/N-CNT-GR and (g) ORR polarization curves of Fe_xN/N-CNT-GR and Pt/C. Reprinted with permission [131]. Copyright 2020, Elsevier.

showed that different carbon layers on MoN(001) led to different hydrogen adsorption ability: both N-doped/B,N-codoped graphene and pristine MoN(001) showed either too strong or too weak H adsorption. However, assembling N-doped/B,N-codoped carbon onto MoN(001) could optimize both the adsorption and desorption of hydrogen on the catalysts (Fig. 13e). Moreover, the electron transfer between different composites (MoN→C→N) induced the carbon atoms to be new active sites for HER. Noh *et al.* [131] loaded Fe_xN nanoparticles in N-doped CNT-graphene (Fe_xN/N-CNT-GR) through a hydrothermal process followed by annealing. Numerous small N-rich FeN nanoparticles were confined by the anchoring and defect sites of carbon support (Fig. 13f). The synergistic effect of Fe_xN (M=Fe, Co) nanoparticles and support created ORR sites with superior durability. Moreover, the 3D porous structure significantly facilitated the oxygen diffusion. Experimental results demonstrated that the Fe_xN/N-CNT-GR catalyst showed an enhanced ORR activity with a half-wave potential of 0.89 V *vs.* RHE comparable to commercial Pt/C in alkaline electrolyte (Fig. 13g).

Interface engineering has also been applied to design nitride-based electrocatalysts [132]. Wang *et al.* [133] engineered a copper-nickel nitride loaded on carbon fiber cloth (Cu_1Ni_2-N/CFC) *via* annealing CuNi-LDH precursor in ammonia. The as-prepared Cu_1Ni_2-N/CFC exhibited a highly open and interconnected nanostructure, which simultaneously improved the mass and charge transfer (Fig. 14a–c). The controlled lattice arrangement between Cu_4N and Ni_3N contributed to increasing the HER active sites. The DOS showed that the Cu_1Ni_2-N was metallic and the d-band center of Cu_4N-Ni_3N was downshifted, which optimized the adsorption of reaction intermediates. Besides, the surface hydroxide species generated during the reaction could serve as the OER active sites. When using hydrazine aqueous solution as the electrolyte, the electrolyzer based on Cu_1Ni_2-N/CFC required a voltage of 0.24 V at 10 mA cm^{-2} with over 75-h stability. As Lai *et al.* [134] reported, strong-interacted NiCoN/C hybrid nanocages were prepared *via* nitridation of chemically etched ZIF-67. The as-prepared material presented a high ECSA and reduced electron transfer resistance. The DFT calculations demonstrated that the interaction between C-sites in carbon layer helped to stabilize the Co and Ni sites, weaken the overbinding of the intermediates and promote the electron transfer (Fig. 14d). Moreover, the (Ni, Co)-N-bonding induced fast electron transfer and promoted the transformation of Co^{2+}→Co^0, which was considered as an ideal site for water adsorption and splitting. Dong *et al.* [135] designed a V-Ni based nitride with 3D hierarchical heterostructure (VN@Ni_3N-Ni/CC) *via in-situ* nitridation of V–Ni–O precursors anchored on carbon cloth. The 3D hierarchical

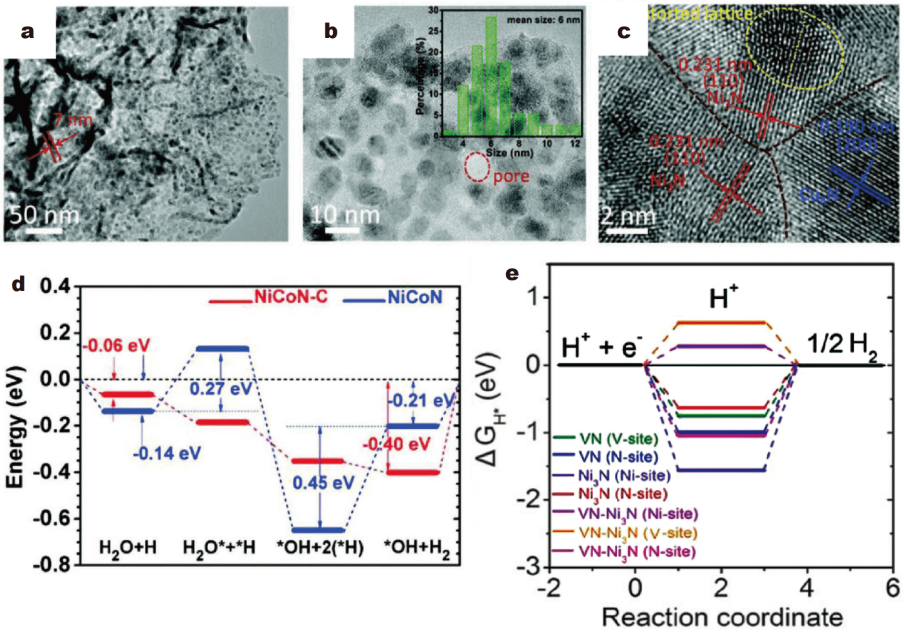

Figure 14 (a,b) TEM and (c) HRTEM images of Cu_1Ni_2-N/CFC. Reprinted with permission [133]. Copyright 2019, Wiley. (d) Alkaline HER free energies on different catalyst surfaces. Reprinted with permission [134]. Copyright 2019, Wiley. (e) HER free energy profile on tdifferent systems. Reprinted with permission [135]. Copyright 2019, American Chemical Society.

nanostructure of the material helped to expose more active sites, promote the interaction between the electrode and electrolyte, and favor the release of the formed gas. The Ni 2p binding energy exhibited a positive shift, indicating a strong electron interaction in VN@Ni_3N–Ni, which significantly optimized the adsorption and desorption of H^*: the ΔG_{H^*} of Ni-site in VN@Ni_3N was much lowered, and therefore served as an excellent HER site (Fig. 14e). As a result, VN@Ni_3N–Ni showed a high catalytic performance with 8, 23, and 32 mV onset potentials in 1.0 mol L^{-1} KOH, 1.0 mol L^{-1} PBS and 0.5 mol L^{-1} H_2SO_4, respectively. Table 5 summarizes the performances of some representative oxide-based electrocatalysts.

CONCLUSIONS AND PERSPECTIVES

From the discussions above, a large number of transition-metal-compound-based nanomaterials have been designed and fabricated for electrocatalytic HER, OER and ORR in recent two years. And many of them have shown promising prospects in replacing noble metal-based catalysts for sustainable energy conversion and storage. To promote the development of electrocatalysts, various strategies have been proposed and applied in fabricating novel electrocatalysts, such as improving the ECSA to expose more catalytic sites, inducing electron redistribution in the surface sites to modify the physiochemical properties of catalysts, increasing the intrinsic activity of active sites *via* tuning the composite/structure and optimizing the adsorption/desorption property of the intermediates, and reducing the resistance to favor the electron transfer during the reaction. As a result, some of the novel TMC-based nanomaterials can even outperform the noble metal-based electrocatalysts.

However, there are still some critical issues to be solved for further development and actual commercialization of TMC-based electrocatalysts: 1) the next-generation sustainable electrochemical energy conversion devices usually involve multi-reactions to simultaneously participate on the anode and cathode. For example, water electrolysis devices require simultaneous HER and OER, while zinc-air batteries require efficient OER and ORR performances on the anode. Therefore, more efforts are needed to develop novel catalysts with multi-functions and further improve the activities and stability to meet the industrialization requirements. 2) During the electrochemical reaction process, the high overpotential and the acid/alkaline electrolytes create a corrosive environment, which could induce strong reconstruction on the surface sites (including the composition, valence state, and phase change). However, most of the simulative crystalline structures in the theoretical calculations are

Table 5 Comparison of the performances of transition metal carbide/nitride-based electrocatalysts for different applications

Catalyst	Substrate	Electrolyte /reaction	Overpotential (mV)@mA cm^{-2}	Tafel slope (mV $decade^{-1}$)	Stability (mA cm^{-2}@h)
Co-NC@Mo_2C [112]	GCE	1.0 mol L^{-1} KOH/HER	99@10	65	1000 cycles
Fe/Fe_5C_2@N-doped carbon [113]	RRDE	0.1 mol L^{-1} KOH/ORR	$E_{1/2}$=0.85 V	57	5000 cycles
Mo_2CT_x nanomeshs [114]	Ni foam	1.0 mol L^{-1} KOH/OER	180@10	66	1.9 V@16
Mo_2C/VC heterojunction [115]	Glassy carbon	0.5 mol L^{-1} H_2SO_4/HER	122@10	43.8	10000 cycles
MoC-Mo_2C/PNCDs [121]	Carbon fiber paper	1.0 mol L^{-1} KOH/HER	121@10	60	10@20
WC-W_2C/PNCDs [121]	Carbon fiber paper	1.0 mol L^{-1} KOH/HER	101@10	90	10@24
mC-Mo-850 [122]	RDE	1.0 mol L^{-1} KOH/HER	173@10	55	10/50/100@16
Ni/Mo_2C-NCNFs [123]	RDE	1.0 mol L^{-1} KOH/HER	143@10	57.8	10@100
Ni/Mo_2C-NCNFs [123]	RDE	1.0 mol L^{-1} KOH/OER	288@10	78.4	10@100
NiNS [125]	Glassy carbon	1.0 mol L^{-1} KOH/HER	197@100	58.8	5000 cycles
Ni_3N/VN [126]	Ni foam	1.0 mol L^{-1} KOH/HER	56@10	47	10@16
FeNi$_3$N/NG [127]	RRDE	1.0 mol L^{-1} KOH/ORR	$E_{1/2}$=0.79 V	78.8	
Cobalt vanadium nitride [128]	Carbon cloth	1.0 mol L^{-1} KOH/HER	118@10	73.6	1.56 V@20
Cu_3N/NF [129]	Ni foam	1.0 mol L^{-1} KOH/OER	286@10	118.5	10@14
Cu_3N/NF [129]	Ni foam	1.0 mol L^{-1} KOH/HER	118@10	122	10@14
h-MoN@BNCNT [130]	Glassy carbon	0.5 mol L^{-1} H_2SO_4/HER	78@10	46	10@24
NiCoN/C [134]	Carbon cloth	1.0 mol L^{-1} KOH/HER	103@10		1000 cycles
VN@Ni_3N–Ni/CC [135]	Carbon cloth	1.0 mol L^{-1} KOH/HER	57@10	40	3000 cycles

ideal models, which are based on the *ex-situ* characterizations such as XRD, HERTM and XPS. Therefore, there is still a gap between the theoretical and actual active sites, which makes it difficult to precisely predict the catalyst performance in the actual electrochemical test using the DFT calculation results. Hence, it is necessary to involve *in-situ* characterizations into the research and clarify the actual physicochemical properties of the active sites during the reaction. And it is clear that combining theoretical calculations and *in-situ* characterizations can greatly contribute to understanding the effect of active sites on the reaction performance and summarizing the structure-performance relationship. In the very recent years, this strategy has been more and more frequently applied in the electrocatalytic research, and the reported *in-situ* characterizations include XRD, XANES, Raman and infrared spectra [136–138]. 3) Currently, most of the TMC-based nanomaterials are prepared *via* a hydro/solvothermal method followed by annealing at a high temperature to increase the crystallinity. Especially, for sulfides, phosphides, nitrides and selenides, the sources of S, P, N and Se are usually toxic and may cause environmental concerns. Moreover, most of the current instruments for the preparation of nanomaterials are still laboratory level and it is difficult for the yield to reach a kilogram level. To realize the future commercialization of these TMC-based catalysts, it is necessary to develop facile preparation methods with massive amount producing ability. 4) Except the self-supported materials, most of the electrocatalysts have to be loaded onto the electrode using polymer binders to ensure strong-enough attachment during long-term operation [139]. However, the use of binders will significantly increase the cost (e.g., the price of Nafion solution (5 wt.% in mixture of lower aliphatic alcohols and water) is ca. 250 USD/25 mL) and cover the surface of the electrocatalysts, which would inhibit the exposure of active sites. Meanwhile, the conductivity will also be affected by the binder and the contact gap between the catalysts and the electrode. Therefore, further development of self-supported electrodes should help to lower the cost and enlarge the amount of active sites and conductivity. 5) Most of the current studies about TMC-based oxygen electrocatalysts are usually tested in alkaline electrolytes, as the acid environment with high overpotential will greatly corrode or dissolve the nanomaterials. It is therefore necessary to design and construct new composites or heterostructures to increase both the activity and stability of electrocatalysts in a wide pH range.

Therefore it is believed that further improvement of TMC-based electrocatalysts can be achieved from the inspirations of recent advances with deep understanding of the fundamental mechanisms and rational design of the composite and structure, which can help to replace the noble metal-based electrocatalysts and explore candidates for electrochemical energy devices.

Received 29 April 2020; accepted 2 July 2020; published online 10 September 2020

1 Chen M, Xiao J, Hua W, *et al.* A cation and anion dual doping strategy for the elevation of titanium redox potential for high-power sodium-ion batteries. Angew Chem Int Ed, 2020, 59: 12076–12083
2 Wang H, Tang Q, Chen Z, *et al.* Recent advances on silica-based nanostructures in photocatalysis. Sci China Mater, 2020, 63: 2189–2205
3 Wang Y, Li Y, Wang Z, *et al.* Reticular chemistry in electrochemical carbon dioxide reduction. Sci China Mater, 2020, 63: 1113–1141
4 Dou S, Wang X, Wang S. Rational design of transition metal-based materials for highly efficient electrocatalysis. Small Methods, 2019, 3: 1800211
5 Li R, Lu Y, Lei K, *et al.* Resumption of the discharged Li-$AgVO_3$ primary batteries for rechargeable Li-O_2 batteries. Acta Chim Sin, 2017, 75: 199–205
6 Sun J, Guo L, Sun X, *et al.* One-dimensional nanostructured pseudocapacitive materials: design, synthesis and applications in supercapacitors. Batteries Supercaps, 2019, 2: 820–841
7 Han X, Cheng F, Chen C, *et al.* A Co_3O_4@MnO_2/Ni nanocomposite as a carbon- and binder-free cathode for rechargeable Li–O_2 batteries. Inorg Chem Front, 2016, 3: 866–871
8 Yu D, Li X, Xu J. Safety regulation of gel electrolytes in electrochemical energy storage devices. Sci China Mater, 2019, 62: 1556–1573
9 Zhu Y, Liu X, Jin S, *et al.* Anionic defect engineering of transition metal oxides for oxygen reduction and evolution reactions. J Mater Chem A, 2019, 7: 5875–5897
10 Seh ZW, Kibsgaard J, Dickens CF, *et al.* Combining theory and experiment in electrocatalysis: Insights into materials design. Science, 2017, 355: eaad4998
11 Huang H, Tu S, Zeng C, *et al.* Macroscopic polarization enhancement promoting photo- and piezoelectric-induced charge separation and molecular oxygen activation. Angew Chem Int Ed, 2017, 56: 11860–11864
12 Xu N, Li X, Li H, *et al.* A novel composite (FMC) to serve as a durable 3D-clam-shaped bifunctional cathode catalyst for both primary and rechargeable zinc-air batteries. Sci Bull, 2017, 62: 1216–1226
13 Ni B, Wu L, Chen R, *et al.* Fe/Co-based nanoparticles encapsulated in heteroatom-doped carbon electrocatalysts for oxygen reduction reaction. Sci China Mater, 2016, 62: 1626–1641
14 Shi Y, Zhang B. Recent advances in transition metal phosphide nanomaterials: synthesis and applications in hydrogen evolution reaction. Chem Soc Rev, 2016, 45: 1529–1541
15 Pan Y, Zhang C, Lin Y, *et al.* Electrocatalyst engineering and structure-activity relationship in hydrogen evolution reaction: From nanostructures to single atoms. Sci China Mater, 2020, 63: 921–948
16 Sun T, Zhang G, Xu D, *et al.* Defect chemistry in 2D materials for

electrocatalysis. Mater Today Energy, 2019, 12: 215–238
17 Wang J, Yue X, Yang Y, *et al.* Earth-abundant transition-metal-based bifunctional catalysts for overall electrochemical water splitting: A review. J Alloys Compd, 2020, 819: 153346
18 Ye G, Gong Y, Lin J, *et al.* Defects engineered monolayer MoS_2 for improved hydrogen evolution reaction. Nano Lett, 2016, 16: 1097–1103
19 Xu L, Jiang Q, Xiao Z, *et al.* Plasma-engraved Co_3O_4 nanosheets with oxygen vacancies and high surface area for the oxygen evolution reaction. Angew Chem, 2016, 128: 5363–5367
20 Wang H, Liu R, Li Y, *et al.* Durable and efficient hollow porous oxide spinel microspheres for oxygen reduction. Joule, 2018, 2: 337–348
21 Zhou H, Yu F, Sun J, *et al.* Highly active catalyst derived from a 3D foam of $Fe(PO_3)_2/Ni_2P$ for extremely efficient water oxidation. Proc Natl Acad Sci USA, 2017, 114: 5607–5611
22 Pei Y, Cheng Y, Chen J, *et al.* Recent developments of transition metal phosphides as catalysts in the energy conversion field. J Mater Chem A, 2018, 6: 23220–23243
23 Sun H, Yan Z, Liu F, *et al.* Self-supported transition-metal-based electrocatalysts for hydrogen and oxygen evolution. Adv Mater, 2020, 32: 1806326
24 Chen Z, Duan X, Wei W, *et al.* Recent advances in transition metal-based electrocatalysts for alkaline hydrogen evolution. J Mater Chem A, 2019, 7: 14971–15005
25 Zou X, Zhang Y. Noble metal-free hydrogen evolution catalysts for water splitting. Chem Soc Rev, 2015, 44: 5148–5180
26 Morales-Guio CG, Stern LA, Hu X. Nanostructured hydrotreating catalysts for electrochemical hydrogen evolution. Chem Soc Rev, 2014, 43: 6555–6569
27 Suen NT, Hung SF, Quan Q, *et al.* Electrocatalysis for the oxygen evolution reaction: recent development and future perspectives. Chem Soc Rev, 2017, 46: 337–365
28 Anantharaj S, Ede SR, Sakthikumar K, *et al.* Recent trends and perspectives in electrochemical water splitting with an emphasis on sulfide, selenide, and phosphide catalysts of Fe, Co, and Ni: A Review. ACS Catal, 2016, 6: 8069–8097
29 Ge X, Sumboja A, Wuu D, *et al.* Oxygen reduction in alkaline media: from mechanisms to recent advances of catalysts. ACS Catal, 2015, 5: 4643–4667
30 Wang Y, Li J, Wei Z. Transition-metal-oxide-based catalysts for the oxygen reduction reaction. J Mater Chem A, 2018, 6: 8194–8209
31 Skúlason E, Tripkovic V, Björketun ME, *et al.* Modeling the electrochemical hydrogen oxidation and evolution reactions on the basis of density functional theory calculations. J Phys Chem C, 2010, 114: 18182–18197
32 Diaz-Morales O, Ledezma-Yanez I, Koper MTM, *et al.* Guidelines for the rational design of Ni-based double hydroxide electrocatalysts for the oxygen evolution reaction. ACS Catal, 2015, 5: 5380–5387
33 Nørskov JK, Rossmeisl J, Logadottir A, *et al.* Origin of the overpotential for oxygen reduction at a fuel-cell cathode. J Phys Chem B, 2004, 108: 17886–17892
34 Zhang T, Wu MY, Yan DY, *et al.* Engineering oxygen vacancy on NiO nanorod arrays for alkaline hydrogen evolution. Nano Energy, 2018, 43: 103–109
35 Xue Y, Sun S, Wang Q, *et al.* Transition metal oxide-based oxygen reduction reaction electrocatalysts for energy conversion systems with aqueous electrolytes. J Mater Chem A, 2018, 6: 10595–10626
36 Teng Y, Wang XD, Liao JF, *et al.* Atomically thin defect-rich Fe-Mn-O hybrid nanosheets as high efficient electrocatalyst for water oxidation. Adv Funct Mater, 2018, 28: 1802463
37 Fu G, Yan X, Chen Y, *et al.* Boosting bifunctional oxygen electrocatalysis with 3D graphene aerogel-supported Ni/MnO particles. Adv Mater, 2018, 30: 1704609
38 Zhou Y, Sun S, Xi S, *et al.* Superexchange effects on oxygen reduction activity of edge-sharing $[Co_xMn_{1-x}O_6]$ octahedra in spinel oxide. Adv Mater, 2018, 30: 1705407
39 Wei C, Sun S, Mandler D, *et al.* Approaches for measuring the surface areas of metal oxide electrocatalysts for determining their intrinsic electrocatalytic activity. Chem Soc Rev, 2019, 48: 2518–2534
40 Liu Q, Hu Z, Chen M, *et al.* Recent progress of layered transition metal oxide cathodes for sodium-ion batteries. Small, 2019, 15: 1805381
41 Han X, He G, He Y, *et al.* Engineering catalytic active sites on cobalt oxide surface for enhanced oxygen electrocatalysis. Adv Energy Mater, 2018, 8: 1702222
42 Lai F, Feng J, Ye X, *et al.* Energy level engineering in transition-metal doped spinel-structured nanosheets for efficient overall water splitting. J Mater Chem A, 2019, 7: 827–833
43 Peng S, Han X, Li L, *et al.* Electronic and defective engineering of electrospun $CaMnO_3$ nanotubes for enhanced oxygen electrocatalysis in rechargeable zinc-air batteries. Adv Energy Mater, 2018, 8: 1800612
44 Li X, Wei J, Li Q, *et al.* Nitrogen-doped cobalt oxide nanostructures derived from cobalt-alanine complexes for high-performance oxygen evolution reactions. Adv Funct Mater, 2018, 28: 1800886
45 Ling T, Zhang T, Ge B, *et al.* Well-dispersed nickel- and zinc-tailored electronic structure of a transition metal oxide for highly active alkaline hydrogen evolution reaction. Adv Mater, 2019, 31: 1807771
46 Zhao Y, Zhang J, Wu W, *et al.* Cobalt-doped MnO_2 ultrathin nanosheets with abundant oxygen vacancies supported on functionalized carbon nanofibers for efficient oxygen evolution. Nano Energy, 2018, 54: 129–137
47 Liu J, Ji Y, Nai J, *et al.* Ultrathin amorphous cobalt–vanadium hydr(oxy)oxide catalysts for the oxygen evolution reaction. Energy Environ Sci, 2018, 11: 1736–1741
48 Chen ZJ, Cao GX, Gan LY, *et al.* Highly dispersed platinum on honeycomb-like NiO@Ni film as a synergistic electrocatalyst for the hydrogen evolution reaction. ACS Catal, 2018, 8: 8866–8872
49 Zheng P, Zhang Y, Dai Z, *et al.* Constructing multifunctional heterostructure of $Fe_2O_3@Ni_3Se_4$ nanotubes. Small, 2018, 14: 1704065
50 Yan Z, Sun H, Chen X, *et al.* Anion insertion enhanced electrodeposition of robust metal hydroxide/oxide electrodes for oxygen evolution. Nat Commun, 2018, 9: 2373
51 Zhang X, Li J, Yang Y, *et al.* $Co_3O_4/Fe_{0.33}Co_{0.66}P$ interface nanowire for enhancing water oxidation catalysis at high current density. Adv Mater, 2018, 30: 1803551
52 Yu ZY, Lang CC, Gao MR, *et al.* Ni–Mo–O nanorod-derived composite catalysts for efficient alkaline water-to-hydrogen conversion *via* urea electrolysis. Energy Environ Sci, 2018, 11: 1890–1897
53 An L, Feng J, Zhang Y, *et al.* Epitaxial heterogeneous interfaces on $N\text{-}NiMoO_4/NiS_2$ nanowires/nanosheets to boost hydrogen and

oxygen production for overall water splitting. Adv Funct Mater, 2019, 29: 1805298
54 Xu H, Shi ZX, Tong YX, *et al.* Porous microrod arrays constructed by carbon-confined NiCo@$NiCoO_2$ core@shell nanoparticles as efficient electrocatalysts for oxygen evolution. Adv Mater, 2018, 30: 1705442
55 Duan Y, Sun S, Sun Y, *et al.* Mastering surface reconstruction of metastable spinel oxides for better water oxidation. Adv Mater, 2019, 31: 1807898
56 Yan Z, Xiao J, Lai W, *et al.* Nickel sulfide nanocrystals on nitrogen-doped porous carbon nanotubes with high-efficiency electrocatalysis for room-temperature sodium-sulfur batteries. Nat Commun, 2019, 10: 4793
57 Yan Y, Xia BY, Xu Z, *et al.* Recent development of molybdenum sulfides as advanced electrocatalysts for hydrogen evolution reaction. ACS Catal, 2014, 4: 1693–1705
58 Yilmaz G, Yang T, Du Y, *et al.* Stimulated electrocatalytic hydrogen evolution activity of MOF-derived MoS_2 basal domains *via* charge injection through surface functionalization and heteroatom doping. Adv Sci, 2019, 6: 1900140
59 Zhu J, Wang ZC, Dai H, *et al.* Boundary activated hydrogen evolution reaction on monolayer MoS_2. Nat Commun, 2019, 10: 1348
60 Zhou G, Shan Y, Wang L, *et al.* Photoinduced semiconductor-metal transition in ultrathin troilite FeS nanosheets to trigger efficient hydrogen evolution. Nat Commun, 2019, 10: 399
61 Zhong J, Wu T, Wu Q, *et al.* N- and S- co-doped graphene sheet-encapsulated Co_9S_8 nanomaterials as excellent electrocatalysts for the oxygen evolution reaction. J Power Sources, 2019, 417: 90–98
62 Guo Y, Park T, Yi JW, *et al.* Nanoarchitectonics for transition-metal-sulfide-based electrocatalysts for water splitting. Adv Mater, 2019, 31: 1807134
63 Kuang P, He M, Zou H, *et al.* 0D/3D MoS_2-NiS_2/N-doped graphene foam composite for efficient overall water splitting. Appl Catal B-Environ, 2019, 254: 15–25
64 Joo J, Kim T, Lee J, *et al.* Morphology-controlled metal sulfides and phosphides for electrochemical water splitting. Adv Mater, 2019, 31: 1806682
65 Dong J, Zhang FQ, Yang Y, *et al.* (003)-Facet-exposed Ni_3S_2 nanoporous thin films on nickel foil for efficient water splitting. Appl Catal B-Environ, 2019, 243: 693–702
66 Li B, Jiang L, Li X, *et al.* Controllable synthesis of nanosized amorphous MoS_x using temporally shaped femtosecond laser for highly efficient electrochemical hydrogen production. Adv Funct Mater, 2019, 29: 1806229
67 Yang H, Wang B, Li H, *et al.* Trimetallic sulfide mesoporous nanospheres as superior electrocatalysts for rechargeable Zn-air batteries. Adv Energy Mater, 2018, 8: 1801839
68 Kong D, Wang Y, Lim YV, *et al.* 3D hierarchical defect-rich $NiMo_3S_4$ nanosheet arrays grown on carbon textiles for high-performance sodium-ion batteries and hydrogen evolution reaction. Nano Energy, 2018, 49: 460–470
69 Qu Y, Yang M, Chai J, *et al.* Facile synthesis of vanadium-doped Ni_3S_2 nanowire arrays as active electrocatalyst for hydrogen evolution reaction. ACS Appl Mater Interfaces, 2017, 9: 5959–5967
70 Muthurasu A, Maruthapandian V, Kim HY. Metal-organic framework derived Co_3O_4/MoS_2 heterostructure for efficient bifunctional electrocatalysts for oxygen evolution reaction and hydrogen evolution reaction. Appl Catal B-Environ, 2019, 248: 202–210
71 Liu Y, Jiang S, Li S, *et al.* Interface engineering of (Ni, Fe)S_2@MoS_2 heterostructures for synergetic electrochemical water splitting. Appl Catal B-Environ, 2019, 247: 107–114
72 Kim M, Anjum MAR, Lee M, *et al.* Activating MoS_2 basal plane with Ni_2P nanoparticles for Pt-like hydrogen evolution reaction in acidic media. Adv Funct Mater, 2019, 29: 1809151
73 Nguyen DC, Tran DT, Doan TLL, *et al.* Rational design of core@shell structured CoS_x@Cu_2MoS_4 hybridized MoS_2/N,S-co-doped graphene as advanced electrocatalyst for water splitting and Zn-air battery. Adv Energy Mater, 2020, 10: 1903289
74 Han X, Zhang W, Ma X, *et al.* Identifying the activation of bimetallic sites in $NiCo_2S_4$@g-C_3N_4-CNT hybrid electrocatalysts for synergistic oxygen reduction and evolution. Adv Mater, 2019, 31: 1808281
75 Cao Y, Zheng X, Zhang H, *et al.* Interface engineering of NiS_2/CoS_2 nanohybrids as bifunctional electrocatalysts for rechargeable solid state Zn-air battery. J Power Sources, 2019, 437: 226893
76 Lu H, Zhang Y, Huang Y, *et al.* Reaction packaging $CoSe_2$ nanoparticles in N-doped carbon polyhedra with bifunctionality for overall water splitting. ACS Appl Mater Interfaces, 2019, 11: 3372–3381
77 Dutta B, Wu Y, Chen J, *et al.* Partial surface selenization of cobalt sulfide microspheres for enhancing the hydrogen evolution reaction. ACS Catal, 2019, 9: 456–465
78 Zheng X, Han X, Cao Y, *et al.* Identifying dense $NiSe_2$/$CoSe_2$ heterointerfaces coupled with surface high-valence bimetallic sites for synergistically enhanced oxygen electrocatalysis. Adv Mater, 2020, 32: 2000607
79 Zou Z, Wang X, Huang J, *et al.* An Fe-doped nickel selenide nanorod/nanosheet hierarchical array for efficient overall water splitting. J Mater Chem A, 2019, 7: 2233–2241
80 Ding J, Wang P, Ji S, *et al.* Mesoporous nickel selenide N-doped carbon as a robust electrocatalyst for overall water splitting. Electrochim Acta, 2019, 300: 93–101
81 Liu Y, Xu Y, Han Y, *et al.* Facile synthesis of $SnSe_2$ nanoparticles supported on graphite nanosheets for improved sodium storage and hydrogen evolution. J Power Sources, 2019, 436: 226860
82 Yu J, Li WJ, Zhang H, *et al.* Metallic $FePSe_3$ nanoparticles anchored on N-doped carbon framework for all-pH hydrogen evolution reaction. Nano Energy, 2019, 57: 222–229
83 Chen J, Pan A, Wang Y, *et al.* Hierarchical mesoporous $MoSe_2$@CoSe/N-doped carbon nanocomposite for sodium ion batteries and hydrogen evolution reaction applications. Energy Storage Mater, 2019, 21: 97–106
84 Shi X, Wang H, Kannan P, *et al.* Rich-grain-boundary of Ni_3Se_2 nanowire arrays as multifunctional electrode for electrochemical energy storage and conversion applications. J Mater Chem A, 2019, 7: 3344–3352
85 Wang S, He P, Jia L, *et al.* Nanocoral-like composite of nickel selenide nanoparticles anchored on two-dimensional multilayered graphitic carbon nitride: A highly efficient electrocatalyst for oxygen evolution reaction. Appl Catal B-Environ, 2019, 243: 463–469
86 Wang X, He J, Yu B, *et al.* $CoSe_2$ nanoparticles embedded MOF-derived Co-N-C nanoflake arrays as efficient and stable electrocatalyst for hydrogen evolution reaction. Appl Catal B-Environ, 2019, 258: 117996
87 Chen P, Xu K, Tao S, *et al.* Phase-transformation engineering in cobalt diselenide realizing enhanced catalytic activity for hydro-

gen evolution in an alkaline medium. Adv Mater, 2016, 28: 7527–7532
88 Deng S, Ai C, Luo M, *et al.* Coupled biphase (1T-2H)-$MoSe_2$ on mold spore carbon for advanced hydrogen evolution reaction. Small, 2019, 15: 1901796
89 Deng S, Yang F, Zhang Q, *et al.* Phase modulation of (1T-2H)-$MoSe_2$/TiC-C shell/core arrays *via* nitrogen doping for highly efficient hydrogen evolution reaction. Adv Mater, 2018, 30: 1802223
90 Zhang X, Zhang YY, Zhang Y, *et al.* Phase-controlled synthesis of 1T-$MoSe_2$/NiSe heterostructure nanowire arrays *via* electronic injection for synergistically enhanced hydrogen evolution. Small Methods, 2019, 3: 1800317
91 Najafi L, Bellani S, Oropesa-Nuñez R, *et al.* Engineered $MoSe_2$-based heterostructures for efficient electrochemical hydrogen evolution reaction. Adv Energy Mater, 2018, 8: 1703212
92 Zhao Y, Jin B, Zheng Y, *et al.* Charge state manipulation of cobalt selenide catalyst for overall seawater electrolysis. Adv Energy Mater, 2018, 8: 1801926
93 Yuan M, Dipazir S, Wang M, *et al.* Polyoxometalate-assisted formation of CoSe/$MoSe_2$ heterostructures with enhanced oxygen evolution activity. J Mater Chem A, 2019, 7: 3317–3326
94 Jing B, You S, Ma Y, *et al.* Fe_3Se_4/FeSe heterojunctions in cornstalk-derived N-doped carbon framework enhance charge transfer and cathodic oxygen reduction reaction to boost bioelectricity generation. Appl Catal B-Environ, 2019, 244: 465–474
95 Wang J, Zheng X, Cao Y, *et al.* Developing indium-based ternary spinel selenides for efficient solid flexible Zn-air batteries and water splitting. ACS Appl Mater Interfaces, 2020, 12: 8115–8123
96 Zhu Y-, Xiao Y, Hua W-, *et al.* Manipulating layered P2@P3 integrated spinel structure evolution for high-performance sodium-ion batteries. Angew Chem Int Ed, 2020, 59: 9299–9304
97 Liu T, Li P, Yao N, *et al.* CoP-doped MOF-based electrocatalyst for pH-universal hydrogen evolution reaction. Angew Chem Int Ed, 2019, 58: 4679–4684
98 Zhao D, Sun K, Cheong WC, *et al.* Synergistically interactive pyridinic-N-MoP sites: identified active centers for enhanced hydrogen evolution in alkaline solution. Angew Chem, 2020, 132: 9067–9075
99 Yu X, Yu ZY, Zhang XL, *et al.* "Superaerophobic" nickel phosphide nanoarray catalyst for efficient hydrogen evolution at ultrahigh current densities. J Am Chem Soc, 2019, 141: 7537–7543
100 Liang Q, Zhong L, Du C, *et al.* Interfacing epitaxial dinickel phosphide to 2D nickel thiophosphate nanosheets for boosting electrocatalytic water splitting. ACS Nano, 2019, 13: 7975–7984
101 Li G, Yang Q, Rao J, *et al. In situ* induction of strain in iron phosphide (FeP_2) catalyst for enhanced hydroxide adsorption and water oxidation. Adv Funct Mater, 2020, 30: 1907791
102 Du H, Xia L, Zhu S, *et al.* Al-doped Ni_2P nanosheet array: a superior and durable electrocatalyst for alkaline hydrogen evolution. Chem Commun, 2018, 54: 2894–2897
103 Cao B, Cheng Y, Hu M, *et al.* Efficient and durable 3D self-supported nitrogen-doped carbon-coupled nickel/cobalt phosphide electrodes: stoichiometric ratio regulated phase- and morphology-dependent overall water splitting performance. Adv Funct Mater, 2019, 29: 1906316
104 Lv X, Li X, Yang C, *et al.* Large-size, porous, ultrathin NiCoP nanosheets for efficient electro/photocatalytic water splitting. Adv Funct Mater, 2020, 30: 1910830
105 Wu Y, Tao X, Qing Y, *et al.* Cr-doped FeNi-P nanoparticles encapsulated into N-doped carbon nanotube as a robust bifunctional catalyst for efficient overall water splitting. Adv Mater, 2019, 31: 1900178
106 Wang MQ, Ye C, Liu H, *et al.* Nanosized metal phosphides embedded in nitrogen-doped porous carbon nanofibers for enhanced hydrogen evolution at all pH values. Angew Chem Int Ed, 2018, 57: 1963–1967
107 Yu SH, Chen W, Wang H, *et al.* Highly stable tungsten disulfide supported on a self-standing nickel phosphide foam as a hybrid electrocatalyst for efficient electrolytic hydrogen evolution. Nano Energy, 2019, 55: 193–202
108 Yang L, Liu R, Jiao L. Electronic redistribution: Construction and modulation of interface engineering on CoP for enhancing overall water splitting. Adv Funct Mater, 2020, 30: 1909618
109 Boppella R, Tan J, Yang W, *et al.* Homologous CoP/NiCoP heterostructure on N-doped carbon for highly efficient and pH-universal hydrogen evolution electrocatalysis. Adv Funct Mater, 2019, 29: 1807976
110 Zhang Y, Wang Y, Wang T, *et al.* Heterostructure of 2D CoP nanosheets/1D carbon nanotubes to significantly boost the alkaline hydrogen evolution. Adv Mater Interfaces, 2020, 7: 1901302
111 Göhl D, Garg A, Paciok P, *et al.* Engineering stable electrocatalysts by synergistic stabilization between carbide cores and Pt shells. Nat Mater, 2020, 19: 287–291
112 Liang Q, Jin H, Wang Z, *et al.* Metal-organic frameworks derived reverse-encapsulation Co-NC@Mo_2C complex for efficient overall water splitting. Nano Energy, 2019, 57: 746–752
113 Song L, Wang T, Li L, *et al.* $Zn_3[Fe(CN)_6]_2$ derived Fe/Fe_5C_2@N-doped carbon as a highly effective oxygen reduction reaction catalyst for zinc-air battery. Appl Catal B-Environ, 2019, 244: 197–205
114 Kou Z, Zhang L, Ma Y, *et al.* 2D carbide nanomeshes and their assembling into 3D microflowers for efficient water splitting. Appl Catal B-Environ, 2019, 243: 678–685
115 Huang C, Miao X, Pi C, *et al.* Mo_2C/VC heterojunction embedded in graphitic carbon network: An advanced electrocatalyst for hydrogen evolution. Nano Energy, 2019, 60: 520–526
116 Gao Q, Zhang W, Shi Z, *et al.* Structural design and electronic modulation of transition-metal-carbide electrocatalysts toward efficient hydrogen evolution. Adv Mater, 2019, 31: 1802880
117 Baek DS, Jung GY, Seo B, *et al.* Ordered mesoporous metastable α-MoC_{1-x} with enhanced water dissociation capability for boosting alkaline hydrogen evolution activity. Adv Funct Mater, 2019, 29: 1901217
118 Han N, Yang KR, Lu Z, *et al.* Nitrogen-doped tungsten carbide nanoarray as an efficient bifunctional electrocatalyst for water splitting in acid. Nat Commun, 2018, 9: 924
119 Karuppannan M, Park JE, Bae HE, *et al.* A nitrogen and fluorine enriched Fe/Fe_3C@C oxygen reduction reaction electrocatalyst for anion/proton exchange membrane fuel cells. Nanoscale, 2020, 12: 2542–2554
120 Lin H, Zhang W, Shi Z, *et al.* Electrospinning hetero-nanofibers of Fe_3C-Mo_2C/nitrogen-doped-carbon as efficient electrocatalysts for hydrogen evolution. ChemSusChem, 2017, 10: 2597–2604
121 Lu XF, Yu L, Zhang J, *et al.* Ultrafine dual-phased carbide nanocrystals confined in porous nitrogen-doped carbon dodecahedrons for efficient hydrogen evolution reaction. Adv Mater, 2019, 31: 1900699
122 Li S, Cheng C, Sagaltchik A, *et al.* Metal-organic precursor-derived mesoporous carbon spheres with homogeneously dis-

tributed molybdenum carbide/nitride nanoparticles for efficient hydrogen evolution in alkaline media. Adv Funct Mater, 2019, 29: 1807419
123 Li M, Zhu Y, Wang H, *et al.* Ni strongly coupled with Mo_2C encapsulated in nitrogen-doped carbon nanofibers as robust bifunctional catalyst for overall water splitting. Adv Energy Mater, 2019, 9: 1803185
124 Peng X, Pi C, Zhang X, *et al.* Recent progress of transition metal nitrides for efficient electrocatalytic water splitting. Sustain Energy Fuels, 2019, 3: 366–381
125 Zhao Y, Jin B, Vasileff A, *et al.* Interfacial nickel nitride/sulfide as a bifunctional electrode for highly efficient overall water/seawater electrolysis. J Mater Chem A, 2019, 7: 8117–8121
126 Zhou P, Xing D, Liu Y, *et al.* Accelerated electrocatalytic hydrogen evolution on non-noble metal containing trinickel nitride by introduction of vanadium nitride. J Mater Chem A, 2019, 7: 5513–5521
127 Liu L, Yan F, Li K, *et al.* Ultrasmall $FeNi_3N$ particles with an exposed active (110) surface anchored on nitrogen-doped graphene for multifunctional electrocatalysts. J Mater Chem A, 2019, 7: 1083–1091
128 Dutta S, Indra A, Feng Y, *et al.* Promoting electrocatalytic overall water splitting with nanohybrid of transition metal nitride-oxynitride. Appl Catal B-Environ, 2019, 241: 521–527
129 Panda C, Menezes PW, Zheng M, *et al. In situ* formation of nanostructured core–shell Cu_3N–CuO to promote alkaline water electrolysis. ACS Energy Lett, 2019, 4: 747–754
130 Miao J, Lang Z, Zhang X, *et al.* Polyoxometalate-derived hexagonal molybdenum nitrides (MXenes) supported by boron, nitrogen codoped carbon nanotubes for efficient electrochemical hydrogen evolution from seawater. Adv Funct Mater, 2018, 28: 1805893
131 Noh WY, Lee JH, Lee JS. Nitrogen-doped carbon nanotube–graphene hybrid stabilizes M_xN (M = Fe, Co) nanoparticles for efficient oxygen reduction reaction. Appl Catal B-Environ, 2020, 268: 118415
132 Hou J, Sun Y, Li Z, *et al.* Electrical behavior and electron transfer modulation of nickel-copper nanoalloys confined in nickel-copper nitrides nanowires array encapsulated in nitrogen-doped carbon framework as robust bifunctional electrocatalyst for overall water splitting. Adv Funct Mater, 2018, 28: 1803278
133 Wang Z, Xu L, Huang F, *et al.* Copper-nickel nitride nanosheets as efficient bifunctional catalysts for hydrazine-assisted electrolytic hydrogen production. Adv Energy Mater, 2019, 9: 1900390
134 Lai J, Huang B, Chao Y, *et al.* Strongly coupled nickel-cobalt nitrides/carbon hybrid nanocages with Pt-like activity for hydrogen evolution catalysis. Adv Mater, 2019, 31: 1805541
135 Dong X, Yan H, Jiao Y, *et al.* 3D hierarchical V–Ni-based nitride heterostructure as a highly efficient pH-universal electrocatalyst for the hydrogen evolution reaction. J Mater Chem A, 2019, 7: 15823–15830
136 Wang J, Kattel S, Hawxhurst CJ, *et al.* Enhancing activity and reducing cost for electrochemical reduction of CO_2 by supporting palladium on metal carbides. Angew Chem Int Ed, 2019, 58: 6271–6275
137 Ortiz Peña N, Ihiawakrim D, Han M, *et al.* Morphological and structural evolution of Co_3O_4 nanoparticles revealed by *in situ* electrochemical transmission electron microscopy during electrocatalytic water oxidation. ACS Nano, 2019, 13: 11372–11381
138 Li X, Wang HY, Yang H, *et al. In situ/operando* characterization techniques to probe the electrochemical reactions for energy conversion. Small Methods, 2018, 2: 1700395
139 Hu Q, Li G, Liu X, *et al.* Superhydrophilic phytic-acid-doped conductive hydrogels as metal-free and binder-free electrocatalysts for efficient water oxidation. Angew Chem Int Ed, 2019, 58: 4318–4322

Acknowledgements This work was supported by the National Natural Science Foundation of China (51804216 and 51972224), the Young Elite Scientists Sponsorship Program by CAST (2018QNRC001) and Tianjin Natural Science Foundation (17JCQNJC02100). Wang J acknowledges the support from China Postdoctoral Science Foundation (2019M661014).

Author contributions Wang J wrote the paper; Wang J and Zhang Z prepared the figures; Ding J, Zhong C and Deng Y revised the manuscript; Han X and Hu W provided the overall concept and revised the manuscript. All authors participated in the discussion.

Conflict of interest The authors declare no conflict of interest.

Xiaopeng Han is an associate professor in the School of Materials Science and Engineering at Tianjin University. He received his BSc from Tianjin University (2010) and PhD from Nankai University (2015), respectively. His current research interests focus on the synthesis and engineering of metal or metal-based functional materials for electrocatalysis and secondary high energy battery applications.

Wenbin Hu is a professor in the Department of Materials Science & Engineering, Tianjin University. He graduated from the Central South University with a BSc degree in 1988. He received his MSc degree from Tianjin University in 1991, and PhD degree from the Central South University in 1994. His research interests focus on the design, synthesis and characterization of advanced nanomaterials for energy storage and conversion applications.

微纳结构过渡金属化合物能源转化电催化剂研究进展

王嘉骏[1], 张昭[1], 丁佳[1], 钟澄[1], 邓意达[1], 韩晓鹏[1*], 胡文彬[1,2*]

摘要 化石能源的快速消耗已导致日益严重的气候问题与能源危机, 因此开发清洁绿色的可持续能源技术对人类社会的发展至关重要. 电化学能源转化与存储器件目前受到广泛关注, 而开发高效廉价的电催化剂则是该类技术发展的重中之重. 在多种电催化剂中, 过渡金属化合物由于其储量丰富、性能优越而被广泛研究. 本文综述了包括氧化物、硫化物、硒化物、磷化物、碳化物及氮化物在内的微纳结构过渡金属化合物电催化剂的近期研究进展, 内容包括各类化合物的可控制备方法、实际电催化应用(析氢、析氧及氧还原)与相关反应机理; 同时讨论了该领域目前存在的挑战与进一步的发展策略. 本文意在介绍过渡金属基电催化剂的最新进展与研究前沿, 从而为进一步开发低成本、高性能的清洁能源电催化剂提供参考与思路.

